Imaging, Spectroscopy and Device fabrication using Scanning Probes

Lalit Yadav

A dissertation submitted for the partial fulfilment of BS-MS dual degree in Science

Indian Institute of Science Education and Research (IISER) Mohali

April 2018

Certificate of Examination

This is to certify that the dissertation titled **Imaging, Spectroscopy and Device fabrication using Scanning Probes** submitted by **Lalit Yadav** (Reg. No. MS13065) for the partial fulfillment of BS-MS dual degree programme of the Institute, has been examined by the thesis committee duly appointed by the Institute. The committee finds the work done by the candidate satisfactory and recommends that the report be accepted.

Dr. Yogesh Singh	Dr. Sanjeev Kumar	Dr. Goutam Sheet
		(Supervisor)

Dated: April 2018

Declaration

The work presented in this dissertation has been carried out by me under the guidance of Dr. Goutam Sheet at the Indian Institute of Science Education and Research Mohali.

This work has not been submitted in part or in full for a degree, a diploma, or a fellowship to any other university or institute. Whenever contributions of others are involved, every effort is made to indicate this clearly, with due acknowledgement of collaborative research and discussions. This thesis is a bonafide record of original work done by me and all sources listed within have been detailed in the bibliography.

Lalit Yadav
(Candidate)

Dated: April 2018

In my capacity as the supervisor of the candidates project work, I certify that the above statements by the candidate are true to the best of my knowledge.

Dr. Goutam Sheet
(Supervisor)

Acknowledgements

Firstly, I would like to express my sincere gratitude to my advisor *Dr. Goutam Sheet* who made the largest difference in my life. It is his enthusiasm for science and constant presence in the lab which has always inspired me to carry out research successfully. I would miss discussing the new ideas over black coffee in the AB corridors.

I would like to thank my thesis committee members for their valuable suggestions and feedback.

This work would not have been possible without the help and support of my labmates. I thank my collaborators *Aastha* and *Suman* for working on the projects together. I also thank *Shekhar*, *Anshu*, *Ritesh*, *Sandeep*, *Soumyadip*, *Soumya*, *Aashi*, *Mamta*, *Gayen da* and *Avtar bhaiya* who were always happy to help me. I am grateful to *Rajeshwari Mam* for the stimulating discussions and guidance. You were always there with a word of encouragement or listening ear. All credits go to my lab mates for making *SPIN* lab a beautiful place to work in. I learned a lot from you all.

I am indebted to *Dr. Leena Aggarwal* for her patience while training me on atomic force microscope (AFM). I thank *Kavita*, *Amit* and *Dr. Yogesh Singh* for providing Na_2IrO_3 and $PdTe_2$ crystals. I dully acknowledge the contribution of *Bhavin* in helping me in Raman spectroscopy measurements and *Renu* for her contribution to graphene project. During the course of my work, I had the pleasure of working with several project students, *Neetu*, *Tanmoy*, *Rishi*, and *Shivam*. Their assistance during the initial part of the work is gratefully acknowledged.

I would like to thank *Pranav* for helping me out in the coding.

I thank my buddies *Prabhat*, *Rupendra*, *Ankit*, *Avinash*, *Vijay* and others who were always there with me in thick and thins of life. I find myself lucky to have friends like you. I would miss all the fun we have had in the last five years.

Finally, I would like to acknowledge the people who mean the world to me, my parents and my sister *Pragya*. I have no suitable words that can adequately describe their everlasting love for me. Thank you *Maa* and *Paa* for showing faith in me and giving me the liberty to choose what I desired.

Abstract

In this thesis work, I have used scanning probe microscopy (SPM) as my primary tool to investigate the physical and electrical properties of solids down to nano-metre range at room temperature and cryogenic temperature. Using atomic force microscope we have have studied the surface properties of Na_2IrO_3 crystal and shown that the surface of crystallites evolves rapidly as elemental sodium effuses out of the interleave planes to the surface and undergo sublimation. Using conductive AFM we recorded a series of topographs and surface current maps simultaneously and found that the modification of the surface leads to change in the electronic properties in a dynamic fashion until the whole system reaches a dynamic equilibrium. These observations are important in the context of the exotic electronic and magnetic properties that the surface of Na_2IrO_3 displays.

We have used scanning tunnelling microscopy and scanning tunnelling spectroscopy to show that superconducting phase in $PdTe_2$, a type II Dirac semi-metal, is conventional in nature. Using Dynes equation we analysed the spectroscopy data and quantitatively estimated the superconducting gap Δ.

We have also fabricated the metal-superconductor soft point contact device using nano hole indention technique and studied the transport properties by varying the magnetic field and temperature. I have also optimised the graphene exfoliation from HOPG for fabricating vanderwaal heterostructure.

Contents

Certificate i

Declaration of Authorship ii

Acknowledgements iii

Abstract iv

List of Figures vii

1 Introduction 1
1.1 Scanning probe microscopy 1
1.1.1 Review of Atomic Force Microscopy (AFM) 2
1.1.2 Modes of operation 5
1.1.2.1 Contact Mode 5
1.1.2.2 Non-Contact Mode 7

2 Dynamic Surface Modification due to Effusion of Na in Na_2IrO_3 10
2.1 Introduction 10
2.2 Experiment and result 11
2.3 Conclusion 16

3 Optimization of single layer Graphene exfoliation 18
3.1 Introduction 18
3.2 Synthesis of graphene 19
3.3 Conclusion 22

4 Artifacts in Atomic Force Microscopy 23
4.1 Artifacts due to tip 23
4.2 Artifacts due to piezo scanners 24
4.3 Artifacts due to electronic noise 25

5 Soft Point Contact Device Fabrication **27**
5.1 Method 28
5.2 Measurements 31

6 Scanning Tunneling Spectroscopy **34**
6.1 Theory 34
6.2 Results 36

A Python code for Dynes fit **38**

Bibliography **41**

List of Figures

1.1 (a) Schematic of an atomic force microscope. (b) The raster scan motion. 2
1.2 Optical lever method for detecting the vertical and lateral deflection of the cantilever. 4
1.3 Interatomic interaction potential vs distance. In contact mode tip is the repulsive regime (blue color) while in non contact mode tip is in the attractive regime (green color). 6
1.4 Deflection of an AFM tip while scanning a step topography. The control signal required to minimize the error signal gives a good representation of the true topography. 6
1.5 Shift in the resonance frequency of the cantilever due to force gradient in the proximity to the sample. The cantilever is vibrated near its intrinsic natural frequency such that any change in the natural frequency due to interaction will cause a drastic change in the amplitude. 7
1.6 Deflection of the cantilever in AC mode while scanning a step topography. Feedback loop tries to minimize the change in amplitude by moving the z actuator. 8

2.1 Evolution of surface topography of a single crystal of Na_2IrO_3 with time. Topographs show the emergence of sodium blobs scanned at an interval of (a)0 hrs (b)10 hrs (c)20 hrs (d)30 hrs (e)40 hrs (f)50 hrs after cleaning 12
2.2 Conductive AFM on an area of 8μm x 8μm by applying a bias of $10V$. (a), (b), (c) and (d) show the topography of the same area and (e), (f), (g) and (h) show corresponding current maps. 13
2.3 Topography of the same scan area showing the emergence of sodium clusters. Images (a), (b), (c) and (d) are observed at an interval of 10 hours each. 14
2.4 (a) Topography of 40μm x 40μm area in non contact mode. (b) Topography of the same area showing both cleaned and uncleaned surfaces. (c) I-V measurements on big sodium blobs (1,2), small sodium blobs (3,4) and clean area (5,6). 15
2.5 Conductive AFM over the same area by applying a bias of 6V. (a), (b), (c) and (d) are the topographs while (e), (f), (g), (h) are the corresponding current maps of four successive scans. 16

2.6 Topography images showing decrease in the size of sodium blobs due to sublimation. (a), (b), (c) and (d) are the snapshots recorded at 15 hours interval. 17

3.1 (a) Lattice structure of graphene (b) Energy spectrum of graphene (c) Zoom-in of the conical energy bands close to one of the Dirac points 19
3.2 Deposition of graphene by micromechanical cleavage of HOPG . . . 19
3.3 Optical image of Si wafer after exfoliation of HOPG. Fig(a) shows graphene crystallites are hidden in haystack of thousand of thick flakes. Fig(b) shows two flakes, inside red boxes, with feeble contrast which might be a few-layer graphene. 20
3.4 AFM images of multilayered graphene flakes. Fig(a,b,c) show a graphene flake of thickness $8nm$ comprising of about 22 monolayers. Crumpling, wrinkling and folding of graphene is also visible. Fig (d,e,f) show the atomic steps in stacked layers. From Fig(e) atomic step can be measured to be around $0.3nm$. 21
3.5 Raman spectra of a multilayer graphene flake using $512nm$ laser. The I_{2D}/I_G ratio is 0.60 which corresponds to atleast 10 layers. . . 22

4.1 Artifacts due to tip. (a) Scan lines formation as the tip drags the loosely attached particles along with it. (b) Repeating triangular artifacts due to tip geometry while scanning nanoparticles. (c) Ghost image artifacts due to multiple heads in the damaged tip. 24
4.2 A bow like background due to non linear behaviour of the piezo . . 24
4.3 Electronic noise 25
4.4 Noise due to interference 26

5.1 Schematic of soft point contact device: superconductor (Nb)- metal (Au) 28
5.2 Nano hole indenter setup. 30
5.3 Resistance vs Temperature dependence. Niobium shows a superconducting transition at 6.5 K 31
5.4 The temperature dependence of critical current peaks in thermal regime. 32
5.5 The magnetic field dependence of the normalised differential resistance (dV/dI) 33

6.1 Evolution of coherence peaks and superconducting dip with increasing temperature 36
6.2 Evolution of coherence peaks and superconducting dip with Γ . . . 36
6.3 Experimental STS data of $PbTe_2$ fitted with Dynes equation. 37

Dedicated to Maa, Paa and Di...

Chapter 1

Introduction

1.1 Scanning probe microscopy

Scanning probe microscopy (SPM) are family of tools used for imaging, measuring and manipulating surfaces from atomic to the micron level[1]. SPM use a physical probe, a sharp tip, that scans the surface back and forth over the sample. When the tip moves in close proximity to the investigated object, the interactions between the tip and the surface provide a 3D topographic image of the surface[2]. The interactions can range from Van der Waals force to magnetic and electrostatic forces and thus can measure physical properties such as magnetic domains, static charge distribution, surface conductivity, localized friction, elastic moduli interaction, etc. This makes SPM a flexible and versatile tool for providing information about different properties of materials.

There are two popular subclasses of scanning probe microscopies- scanning tunneling microscopy (STM) and atomic force microscopy (AFM). There is a subtle difference in the way each of them works. While STM uses quantum tunneling to image the surface at the atomic level and can also perform scanning tunneling spectroscopy (STS) and probe the local density of states (LDOS), AFM measures the small force between the surface and the tip which is then used to extract the information about the local physical properties of the surface. The development of these two microscopes is considered as a revolution as they allow the visual characterization of surface structure and measure the crucial sample properties at nano and atomic length scale[1].

1.1.1 Review of Atomic Force Microscopy (AFM)

Atomic Force Microscopy (AFM) is a novel technique for high-resolution imaging of conducting as well as non-conducting surfaces. FIGURE 1.1(a) shows the standard layout of an AFM. AFM consists of a probe tip mounted on the end of a cantilever which senses the interaction force between the sample surface and the sharp tip. This force causes a deflection of the cantilever and this deflection is detected using the optical lever method where a laser beam is reflected from the top of the cantilever into a photodetector. The deflection signal from the optical detector is compared to a set point, denoting the imaging force, and this difference is minimized using a feedback loop. The control signal is used as an estimate of the surface property. The tip scans the surface in a raster fashion (FIGURE 1.1(b)) and thus gives a property (eg. topography) map along the surface.

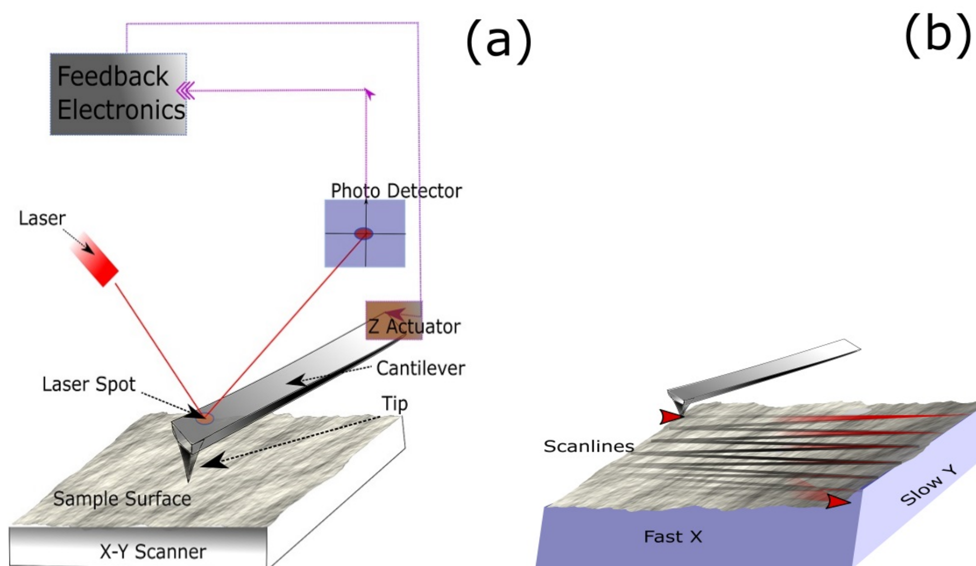

FIGURE 1.1: (a) Schematic of an atomic force microscope. (b) The raster scan motion.

Tip sample interaction

The interaction between the tip and the sample can be represented by the Lennard-Jones potential model[3]

$$F(r) = 4\epsilon[-\frac{\sigma^7}{r^7} + \frac{\sigma^{13}}{r^{13}}] \tag{1.1}$$

where σ is an interaction parameter, r is the distance between the tip and the sample, and ϵ is a constant which depends on the geometry and material of the tip and the sample. The first term $-\frac{\sigma^7}{r^7}$ is the Van der Waals interaction term that characterizes the attractive force between the atoms of tip and sample. The contribution of Van der Waals force becomes prevalent when the separation distance is less than 10 nm. However, at a separation smaller than 1 Å, the overlap of electron clouds and ionic interaction causes strong repulsion between atoms of cantilever and sample surface. This repulsive interaction is captured in the second term $\frac{\sigma^{13}}{r^{13}}$ of Lennard-Jones model. The forces between the tip of the cantilever and the sample are in the range of $10^{-7} - 10^{-12}$ N. In order to produce a deflection significant enough to be detectable, micro-cantilevers with spring constant k less than .001 N/m are used. Further, to measure such a small force precisely it is necessary for the cantilever probe to be insensitive to the surrounding vibrations. The noise from the sources such as building vibrations has a power spectral density significant in the frequency range of 0-2 kHz[3]. Hence, cantilevers with natural frequency more than 2 kHz are used and have dimensions around 100 x 10 x 2 um.

Optical deflection detection

The deflection of the cantilever is detected using optical lever method. A laser beam, having a wavelength of 860 nm, is focussed and reflected off of the back side of the cantilever and finally falls on a segmented photo-diode (Figure 1.2). The segmented photo diode has four quadrants and each quadrant generates a voltage depending on the intensity of light falling on it. As the cantilever deflects, vertically or laterally, the laser spot moves on the detector. Before beginning any experiment, the laser spot is centred at the origin. During the experiment, the vertical deflection is calculated by finding the difference between the voltage signal of upper and bottom quadrant:

$$VerticalDeflection = (V_A + V_B) - (V_c + V_D) \tag{1.2}$$

Similarly for lateral deflection, which corresponds to torsional mode of the cantilever, following operation is performed digitally:

$$LateralDeflection = (V_A + V_C) - (V_B + V_D) \tag{1.3}$$

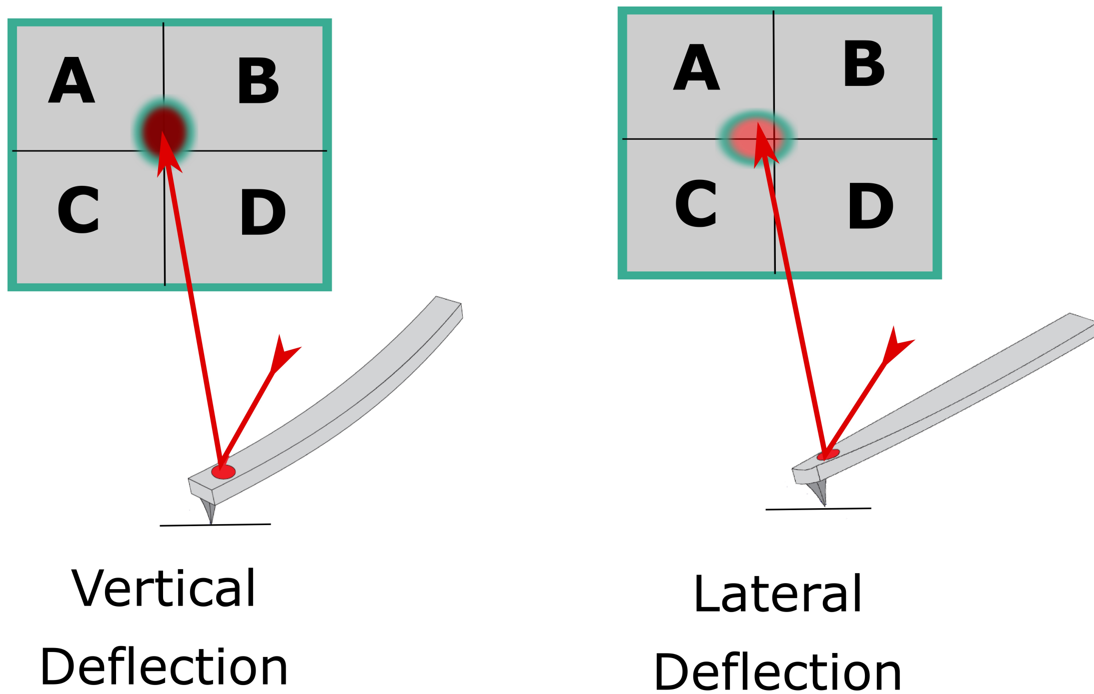

FIGURE 1.2: Optical lever method for detecting the vertical and lateral deflection of the cantilever.

XYZ motion

AFM uses a piezo-based actuation for sample positioning and motion control. The sample is kept on a scanner stage which can move laterally in X and Y direction beneath the tip. This stage contains flexure based translation stages and high-resolution position sensor. The maximum range of scan area in MFP-3D AFM is 90 μm[4]. The vertical (Z) motion of the tip is controlled by a piezo stack in the cantilever assembly.

Feedback loop

In atomic force microscopy, there are several operational modes, like contact mode and AC mode, used for scanning the sample. The details of the operational modes are discussed in the next section. In each of these modes, there is a parameter that serves as a setpoint. For instance, in contact mode, the feedback parameter is a deflection of the cantilever while in AC mode the oscillation amplitude of the cantilever serves as a feedback parameter. During scanning, feedback loop tries to minimize the change in the feedback parameter from its setpoint value by adjusting the z-piezo to move the cantilever probe towards or away from the sample. Thus, the movement of the z-piezo directly gives the height information. The feedback loop is implemented using the proportional-integral-derivative (PID) control, where integral gain plays the most crucial role in optimization of the feedback. If the gain is set too low, the PID loop will not be able to keep track of setpoint on the other hand if the gain is too high, noise signal will amplify strongly. The efficacy of feedback loop also depends on the scan rate. For a fast scan speed, PID loop will not have sufficient time to react and adjust the feedback parameter to maintain the setpoint, and consequently, the topography calculated from z piezo movement will be inaccurate at slopes and near edges. However, for a very slow scan rate, their is no problem with the feedback but it increases the acquisition time which might make the measurement sensitive to thermal drift in the scan piezo.

1.1.2 Modes of operation

1.1.2.1 Contact Mode

In contact mode, the tip is dragged across the surface while raster scanning the sample. The interaction corresponds to the regime where tip-sample separation is very small and tip experiences strong repulsive Coulombic interaction (FIGURE 1.3). Here deflection of the cantilever serves as a feedback parameter which is related to how hard the tip pushes against the surface. In Figure 1.4, deflection feedback is used to image a step topography. When the tip is over the flat area, feedback maintains the deflection at the setpoint. As the tip approaches the step, cantilever bends increasing the deflection above the setpoint. This change in deflection is seen as an error by the controller which gives a control signal that moves

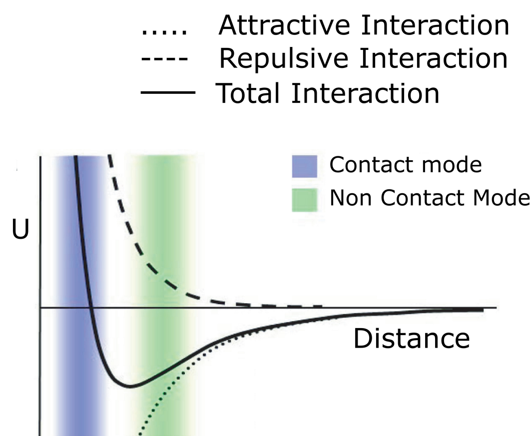

FIGURE 1.3: Interatomic interaction potential vs distance. In contact mode tip is the repulsive regime (blue color) while in non contact mode tip is in the attractive regime (green color).

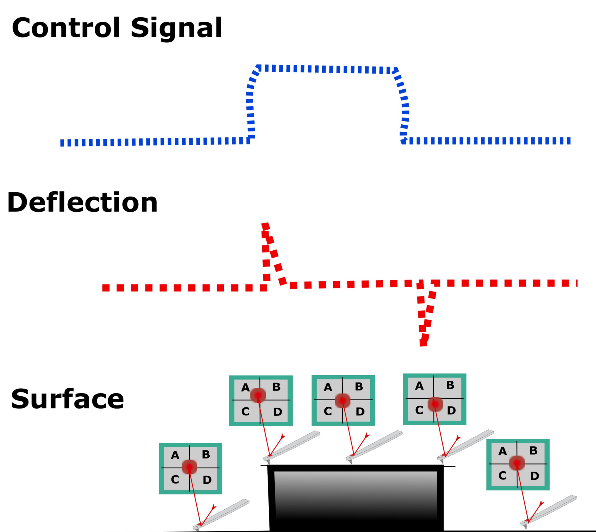

FIGURE 1.4: Deflection of an AFM tip while scanning a step topography. The control signal required to minimize the error signal gives a good representation of the true topography.

the z piezo away from the surface to revert the deflection back to the setpoint. As the surface drops away, deflection once again moves away from the setpoint in opposite direction. Once again, control loop responds to minimize this by giving a control signal that moves the z piezo towards the surface and deflection once again reverts to its nominal value. In this way, control signal itself becomes a representation of the surface.

1.1.2.2 Non-Contact Mode

In Non-Contact (A.C) mode the cantilever is vibrated in the proximity of the surface near its resonant frequency[4]. The non-contact regime is shown in the FIGURE 1.3. The amplitude of the vibrating cantilever is such that it comes in intermittent contact with the surface once in every cycle. When the tip is brought near to the surface, the oscillation amplitude, phase, and frequency are modulated which can be used as a feedback parameter to extract the information about the surface[5].

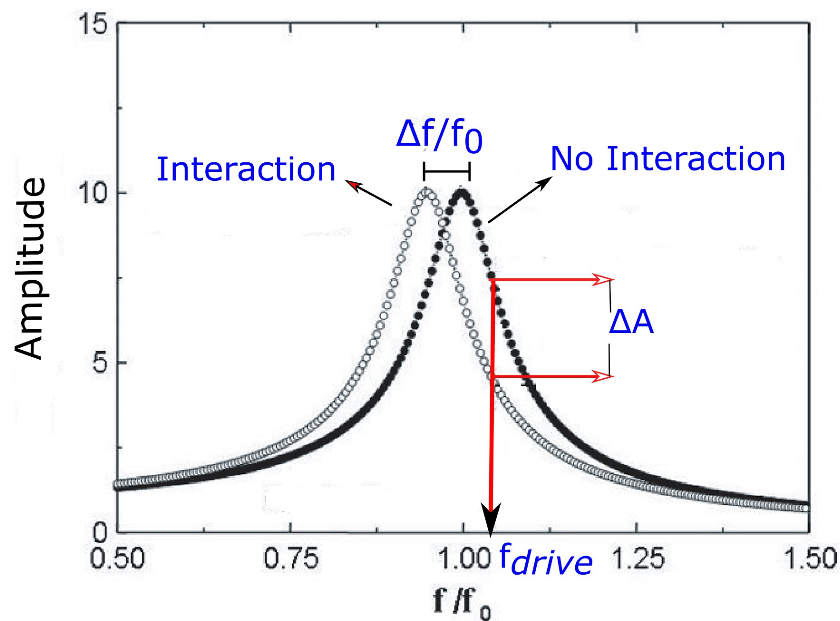

FIGURE 1.5: Shift in the resonance frequency of the cantilever due to force gradient in the proximity to the sample. The cantilever is vibrated near its intrinsic natural frequency such that any change in the natural frequency due to interaction will cause a drastic change in the amplitude.

Unlike contact mode, this method is sensitive to force gradient rather than to the interaction forces themselves[6]. The presence of a force gradient $F^{'} = \partial F_z/\partial z$ shifts the spring constant of the cantilever from its intrinsic spring constant (k_0) to

$$k_{eff} = k_0 - F^{'} \tag{1.4}$$

Therefore, an attractive tip-surface force interaction with $F' > 0$ will soften the effective spring constant and therefore will lead to a decrease of the resonant frequency, whereas a repulsive force, $F' < 0$, will strengthen the spring constant and thereby increasing the resonant frequency[7].

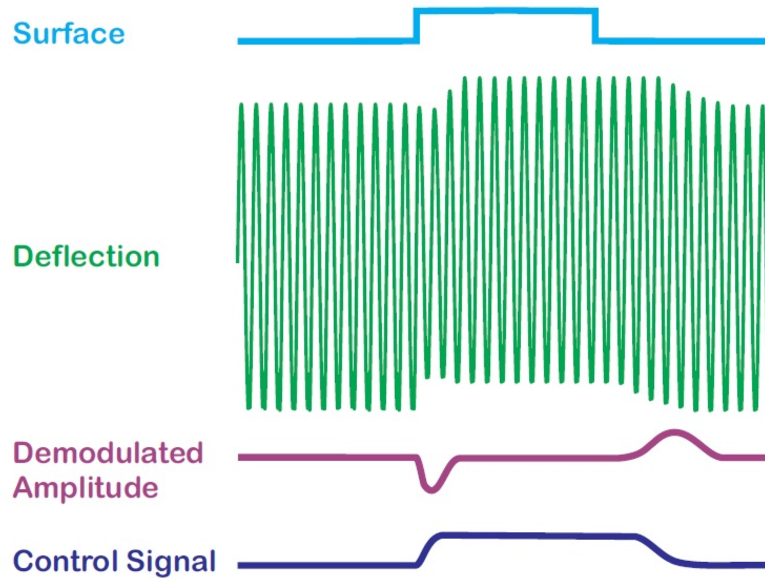

FIGURE 1.6: Deflection of the cantilever in AC mode while scanning a step topography. Feedback loop tries to minimize the change in amplitude by moving the z actuator.

In order to implement AC mode, the cantilever is mechanically oscillated by a small piezoelectric actuator located near the cantilever chip, and the optical detector (segmented photodiode) senses the oscillatory motion of the cantilever from the corresponding oscillation in the laser spot. The acquisition of oscillating voltage signal generated at the photodiode is acquired using 5 MHz ADC which is then routed to a lock-in amplifier which retrieves the amplitude and phase with respect to drive signal. When the cantilever is away from the sample, it is tuned at its first resonance by mechanically vibrating it over a range of frequency using the piezo and noticing the amplitude response of the cantilever (FIGURE 1.5). Once intrinsic fundamental frequency (f_0) of the cantilever is found it driven near this frequency for rest of the experiment. At this point, driving frequency (f_{drive}) and cantilever's resonance frequency (f_0)are almost same and there is no phase difference between them. However, as the vibrating cantilever is approached near the sample and it begins to experience the attractive force, the effective resonant frequency (f_{eff}) will decrease due to the force gradient as discussed earlier. The

cantilever is now being driven at a frequency higher than its new resonance frequency (f_{eff}). From the graph, it can be seen that the amplitude change (ΔA) at f_{drive} (=f_0) becomes very large even for a small change in intrinsic frequency. The change in amplitude (ΔA) at a given frequency is measured and is used as an error signal by the feedback loop (FIGURE 1.6). Here, a set point amplitude $A_{setpoint}$, smaller than free air amplitude, is given to the controller which maintains the setpoint by moving the cantilever up and down using the Z piezo. The control signal that regulates the z peizo provides a measure of the sample topography. This is called as amplitude modulation (AM) AFM. Similar to amplitude, frequency and phase can also be used as a feedback parameter.

Chapter 2

Dynamic Surface Modification due to Effusion of Na in Na_2IrO_3

The honeycomb lattice iridate Na_2IrO_3 shows frustrated magnetism and can potentially display Kitaev-like exchange interactions. Recently, it was shown that the electronic properties of the surface of crystalline Na_2IrO_3 can be tuned by Ar plasma treatment in a controlled manner leading to various phases of matter ranging from a fully gapped to a metallic surface, where the possibility of a charge-density wave (CDW) like transition has been suggested. Here, through direct imaging with an atomic force microscope (AFM) in air, we show that the surface of crystalline Na_2IrO_3 evolves rapidly as elemental Na effuses out of the interleave planes to the surface and undergoes sublimation thereby disappearing from the surface gradually over time. Using conductive AFM we recorded a series of topographs and surface current maps simultaneously and found that the modification of the surface leads to change in the electronic properties in a dynamic fashion until the whole system reaches a dynamic equilibrium. These observations are important in the context of the exotic electronic and magnetic properties that the surface of Na_2IrO_3 displays.

2.1 Introduction

Na_2IrO_3 has been recognized as a promising playground for studying various strongly correlated phenomena[8–10]. Owing to its potential for showing novel ground states driven by the interplay of spin orbit coupling and strong electron

correlations[11–14], it has drawn considerable attention of the condensed matter community and inspired a great deal of theoretical and experimental efforts[8, 15–19]. Na_2IrO_3 has a layered honeycomb structure where oxygen mediated super-exchange between the Ir^{4+} moments is expected to result in practical realization of the Kitaev-Heisenberg models[12, 20]. Depending on the relative strength of the spin-orbit coupling term in the Hamiltonian, it can show different ground states including conventional Neel order and quantum spin liquid behaviour with excitations comprising of the hitherto elusive Majorana fermions [9, 17, 21, 22]. Under certain conditions, Na_2IrO_3 has also been proposed to be a topological insulator, a material with a bulk band gap and topologically protected conducting surface states thereby becoming a possible candidate to show quantum spin Hall (QSH) effect at relatively higher temperatures[23, 24]. As expected, the physical properties of Na_2IrO_3 depend on variation of the crystal structure, especially the change in interlayer distance and the nearest neighbour interaction strength[25]. First principle calculations based on an effective tight binding model have shown that a small change in the interlayer distance of Na_2IrO_3 or interaction strength can drive a regular band insulator phase of Na_2IrO_3 to a topological insulating phase through a quantum phase transition[25]. On experimental side, recently it has been reported that the electronic properties of the surface of Na_2IrO_3 single crystals can be tuned by doping through Ar plasma treatment in a controlled manner ranging from a fully gapped to a metallic surface, where the possibility of a charge-density wave (CDW) like instability is also speculated. Hence, it is important to study the surface properties[26] of Na_2IrO_3 crystals in detail. In this paper, we report detailed investigation of the physical, chemical and electronic properties of the surface of high quality Na_2IrO_3 crystals using scanning probe microscopy (SPM) in various modes.

2.2 Experiment and result

High quality single crystals of Na_2IrO_3 were used for the measurements presented in this paper. The crystals were available in the form of flakes with layers that can be easily cleaved mechanically[8]. The freshly cleaved samples were mounted on the sample stage of an atomic force microscope (MFP 3D of Asylum Research) within 2-3 minutes of cleaving and the cleaved surfaces were imaged in non-contact mode using Si cantilevers with Pt-Ir coating. The spring constant of the cantilevers

varied in a small range around 1.0 N/m. An AFM topograph of a freshly cleaved sample surface is shown in Figure 1(a). The tiny granular structures are blobs of metallic sodium (Na) that have effused out from the layers underneath. The average size of the grains is approximately 8 nm and they continuously grow in size. As shown in Figure 1(b), the size of the blobs have almost doubled after 10 hours and the average size of the grains are seen to be approximately 15 nm. Beyond 10 hours, some of the blobs started coalescing with each other thereby giving rise to a distribution of particle size over the same scan area. Several blobs with average size larger than 20 nm can be seen to have grown after 20 hours of continuous scanning (Figure 1(c)). The size of the grains keeps growing and as shown in Figure 1(d) the average size of the blobs have become more than 30 nm after 30 hours and the coalescing effect is more prominently visible in images captured after 40 hours (figure 1(e)) and 50 hours (figure 1(f)) of cleaving. Imaging of the same area was continuously done for 70 hours and the gradual increase in blob size can be clearly seen in the movie file provided as supplemental material. It can be seen that the blob size does not change noticeably beyond 50 hours.

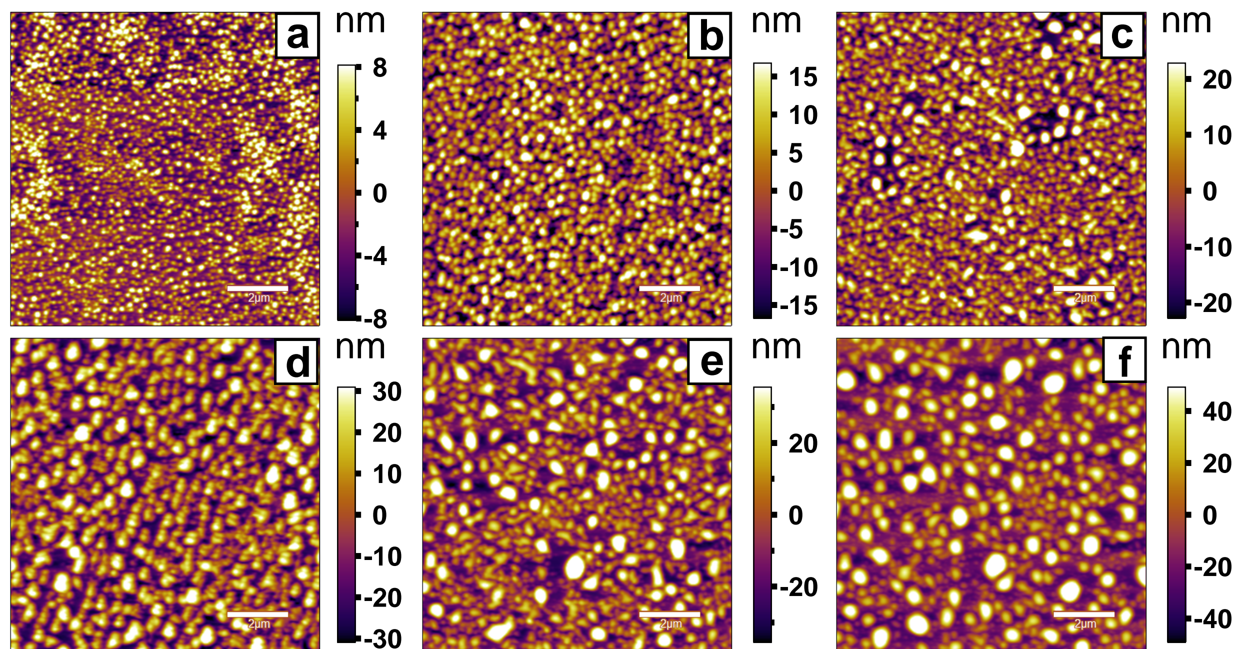

FIGURE 2.1: Evolution of surface topography of a single crystal of Na_2IrO_3 with time. Topographs show the emergence of sodium blobs scanned at an interval of (a)0 hrs (b)10 hrs (c)20 hrs (d)30 hrs (e)40 hrs (f)50 hrs after cleaning

EDX analysis of the surface revealed that while in the area of the surface free of blobs, the ratio of Na and Ir was 2:1 as expected for Na_2IrO_3, the amount of Ir on

the blobs is negligible compared to that of Na. Since EDX is a surface sensitive technique, it can be inferred that the blobs are primarily composed of sodium and the absence of Iridium points towards the fact that elemental sodium has effused out from the layers underneath.

The effusing Na clusters cover the entire surface sufficiently long time after cleaving and it is natural to expect that they will contribute to surface conductivity of the crystal. In order to check whether the blobs on the top surface are electrically connected to the bottom surface, we performed conductivity mapping of the top surface of crystal. For such experiments, the bottom surface of the sample was grounded and a conducting tip, mounted at the end of a soft cantilever, was brought in contact with the top surface. A voltage bias of 10V was applied to the tip and local current variations along with topography were recorded. A current map corresponding to a topography of 8μm x 8μm area (Figure 2(a)) is shown in Figure 2(e).

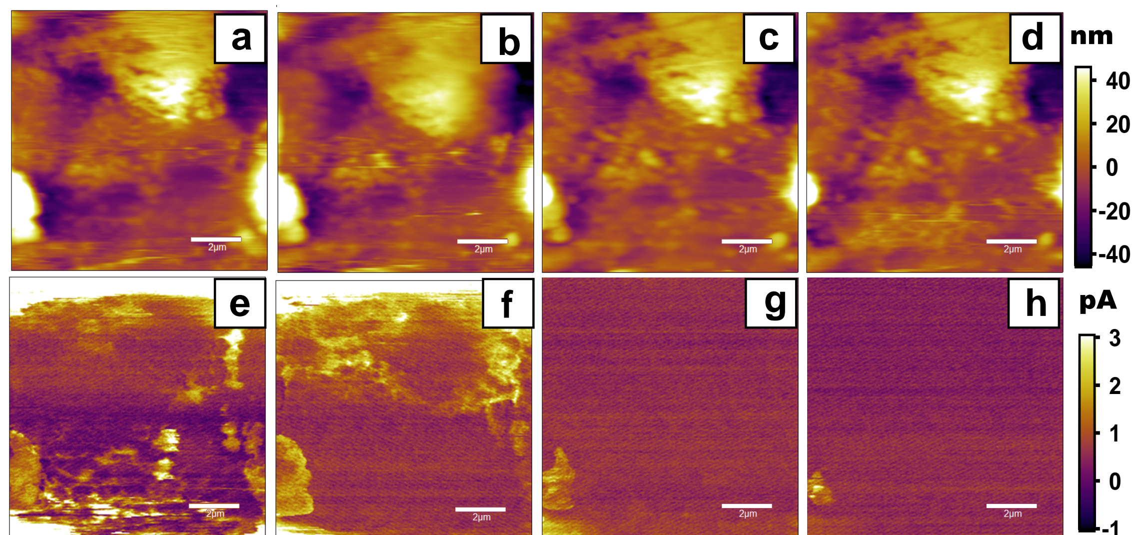

FIGURE 2.2: Conductive AFM on an area of 8μm x 8μm by applying a bias of 10V. (a), (b), (c) and (d) show the topography of the same area and (e), (f), (g) and (h) show corresponding current maps.

The bright regions in the current map correspond to the areas having more conductivity as compared to the dark regions. This means, sites having blobs of elemental sodium show higher conductivity in contrast to the background. Figure 2(b) and 2(c) are the topographs after first conductance map. Here it can be observed that as the tip scans the surface in contact mode, it modifies the surface by dragging the sodium to the edges of the scan area, thereby cleaning the area. Removal of

sodium blobs from the area is clearly seen in the current maps (Figure 2(f) and Figure 2(g)) where a sharp decrease in current is observed compared to that seen during first scan in contact mode. After four subsequent scans, most of the effused sodium was removed (Figure 2(d)) from the scan area and consequently current dropped to zero (Figure 2(h)).

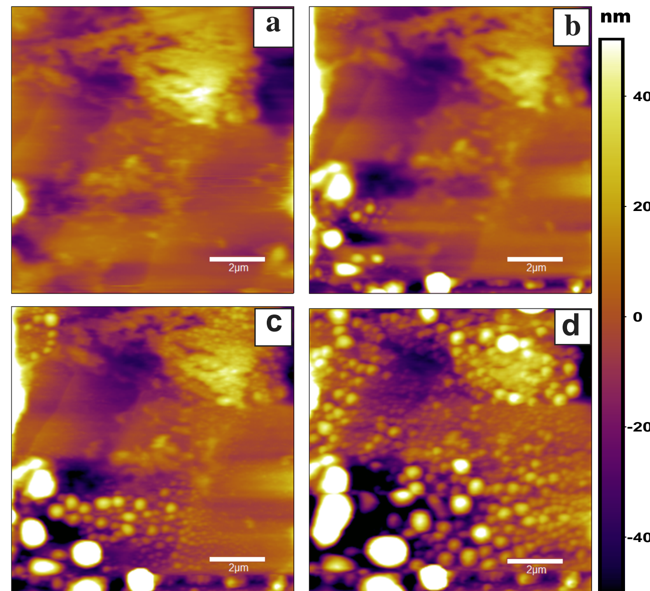

FIGURE 2.3: Topography of the same scan area showing the emergence of sodium clusters. Images (a), (b), (c) and (d) are observed at an interval of 10 hours each.

In order to further investigate the dynamics of the surface, we monitored the time evolution of the topographic features in the area scanned during the previous conductivity measurements (Figure 3(a)) from where Na blobs were removed by the tip. This was done continuously for the next 40 hours. After 10 hours of scanning, we observed sodium blobs emerging from the bottom left corner of the area under investigation (Figure 3(b)). The size of the blobs gradually grew in the next 10 hours (Figure 3(c)). Fresh sodium blobs continued to emerge on the surface in other parts of the scan area and spread over the entire surface as it can be seen in the image captured after 40 hours (Figure 3(d)). This observation, as it is clear in the supplementary video-2, supports the idea that the elemental sodium continuously effuses from the layers below the surface in Na_2IrO_3.

We measured current vs voltage dependence of the surface at sites with different size of sodium blobs. For that, we took a fresh area of 40μm x 40μm (Figure

2(a)) and cleaned a part of it(25μm x 25μm) by bringing the tip in contact with the sample(Figure 2(b)). Sodium present in the cleaned area got accumulated at the edges. We performed I-V measurements on big sodium blobs (point 1 and point 2), small sodium blobs (point 3 and point 4) and the clean area (point 5 and point 6). In each of the measurement bias voltage was swept from 0V to 1V and the resultant I-V curve showed non linear dependence (Figure 2(C)). From the analysis of I-V curve it can be clearly seen that there is a dramatic increase in the current for sodium rich sites than those without sodium.

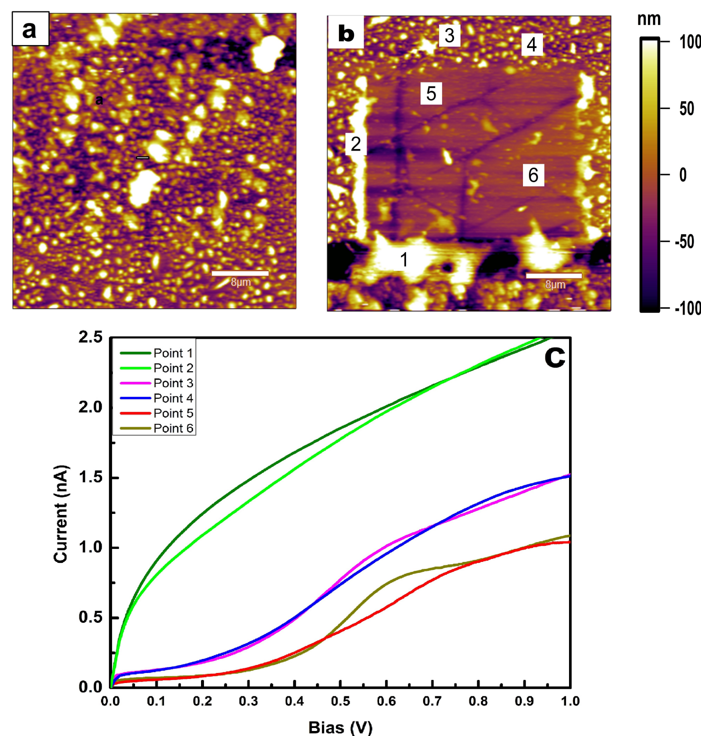

FIGURE 2.4: (a) Topography of 40μm x 40μm area in non contact mode. (b) Topography of the same area showing both cleaned and uncleaned surfaces. (c) I-V measurements on big sodium blobs (1,2), small sodium blobs (3,4) and clean area (5,6).

After around 50 hours, the growth of the blobs almost stopped possibly due to a dynamic equilibrium established between effusion and spontaneous sublimation of Na. After this situation was achieved, we performed conductive AFM measurements again by applying a voltage bias of 6V over the same area and obtained the current distribution as shown in Fig 4. In Fig 4(e), a current of 1-2pA is observed from the surface wherever sodium is present. As the Na is removed from the area by the tip due to multiple scans, the current dropped to zero again as shown in Fig 4(h).

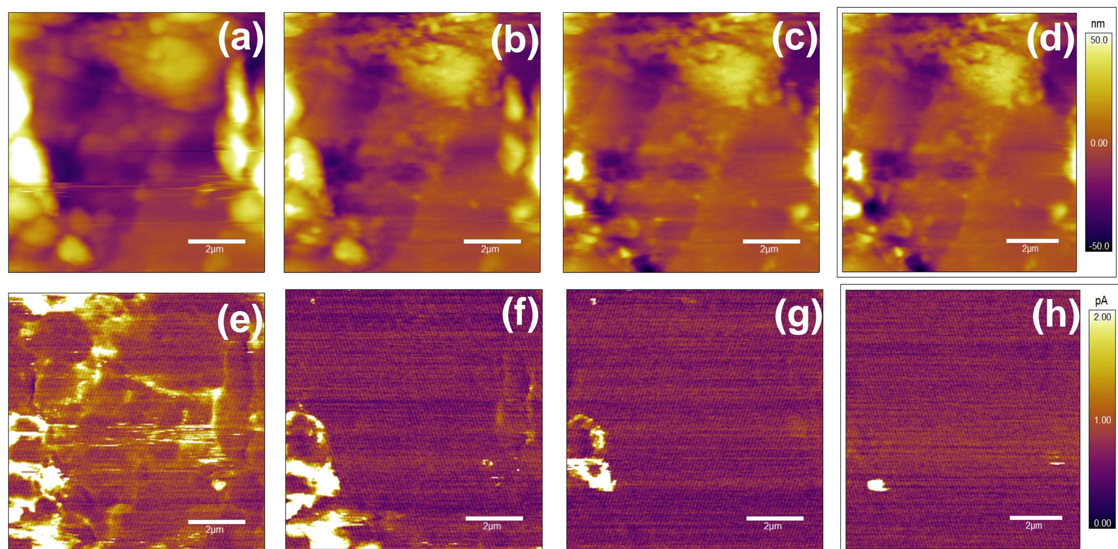

FIGURE 2.5: Conductive AFM over the same area by applying a bias of 6V. (a), (b), (c) and (d) are the topographs while (e), (f), (g), (h) are the corresponding current maps of four successive scans.

The Na clusters formed on the area that was previously cleaned by the tip start disappearing from the surface after some time due to continued sublimation and exhaustion of effusive Na and as a consequence the blob size start reducing (Figure 5). The images (a), (b), (c), (d) in Fig 5 are the snapshots after 15 hours interval. The brighter grains visible in Fig 5(a) turn faint in the Fig 5(b) and (c) and finally disappear into background (Fig 5(d)).

2.3 Conclusion

In conclusion, we have demonstrated that the surface of Na_2IrO_3 crystals become Na rich due to effusion of Na from the bulk. The effusing sodium get accumulated in the form of clusters on the crystal surface. Therefore, the observation of the exotic properties that Na_2IrO_3 can potentially exhibit might be prohibited due to the effusion of Na to the surface. We have also shown that the Na clusters on the surface can be cleaned mechanically. From scanning probe microscopy in different modes we have shown that such clusters of Na make the surface significantly conductive. If the crystals are cooled down right after cleaning, the effusion process can be minimized and its intrinsic properties can be retained for investigation.

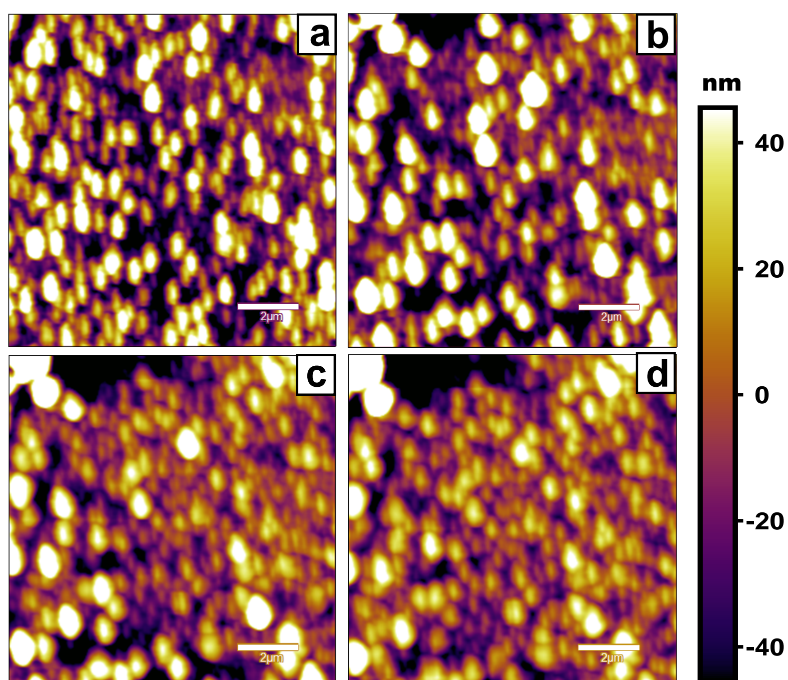

Figure 2.6: Topography images showing decrease in the size of sodium blobs due to sublimation. (a), (b), (c) and (d) are the snapshots recorded at 15 hours interval.

Chapter 3

Optimization of single layer Graphene exfoliation

The recent success in extracting graphene from highly ordered pyrolytic graphite (HOPG) has attracted huge interest in understanding its properties experimentally. The microfabrication of graphene based devices, for experimental studies, relies on the fact that graphene crystallites can be visualised using an optical microscope if placed on the top of silicon wafer. However, detection of graphene among the haystack of thousands of graphite flakes is still a challenging task, comprising of several steps which requires optimisation and expertise. We were able to successfully identify and characterize graphene flakes of thickness 8nm. We have also synthesized turbostratic wrinkle graphite from naphthalene. Once it is possible to isolate a few layer graphene (thickness $\leq 2nm$), we will focus on fabrication of graphene-superconductor devices and study their transport properties.

3.1 Introduction

Graphene is a monolayer of carbon atoms packed tightly in a 2D honeycomb lattice (FIGURE 3.1 (a)). It is the basic building block of graphite. It exhibits high crystal quality, ballistic transport on a submicron scale (even under ambient conditions) and its charge carriers accurately mimic massless Dirac fermions[27].

There are two popular ways of making graphene : chemical vapour deposition (CVD) and mechanical exfoliation of HOPG. However, only the latter produces

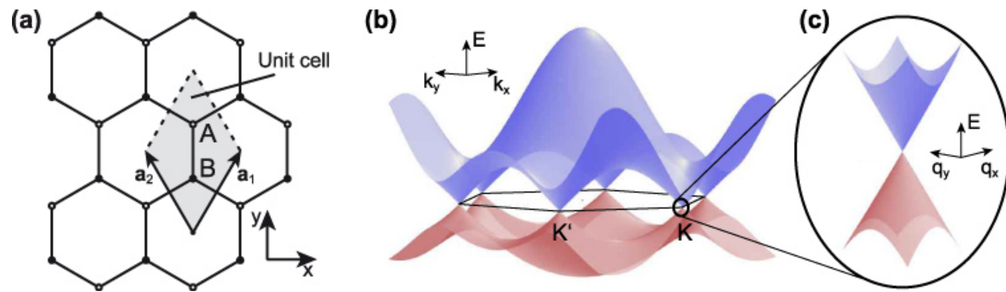

FIGURE 3.1: (a) Lattice structure of graphene (b) Energy spectrum of graphene (c) Zoom-in of the conical energy bands close to one of the Dirac points

high quality graphene samples. The first step of fabrication of graphene-based devices is to identify graphene flakes with different number of layers and determine there relative position on the wafer with respect to the pre-formed alignment marks. We have used optical microscope, AFM and Raman for identification of the flakes.

3.2 Synthesis of graphene

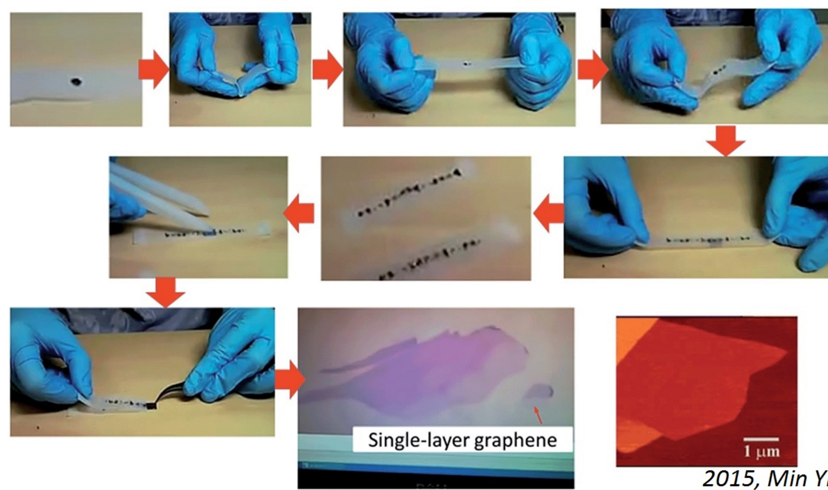

FIGURE 3.2: Deposition of graphene by micromechanical cleavage of HOPG

We have used highly oriented pyrolytic graphite (HOPG) for exfoliating graphene layers. In this method, one takes a scotch tape and press it against the HOPG surface and peels of several layers of graphite and then one folds and opens the the tape several times which leads to the thinning of the graphite layers. After repeating it for several times, in principal, there would be a single layer graphene among other thicker flakes on the scotch tape as shown in FIGURE 3.2. In the next step silicon substrate is put on the tape, slightly pressed on and carefully

removed. FIGURE 3.3 shows the image of Si substrate after flakes has been transferred. Identification of the single layer graphene is a challenging task as the single layer is hiding in the haystack of thousand of graphite flakes and is almost invisible. However, if graphene is placed on a silicon wafer having 300 nm of silicon oxide layer then there is a very weak interference like contrast with respect to empty wafer. So one need to look for the weakest contrast flake. Using trial and error method we were able to detect and locate graphene flakes upto 20 layers. We used atomic force microscopy and Raman spectroscopy for characterization.

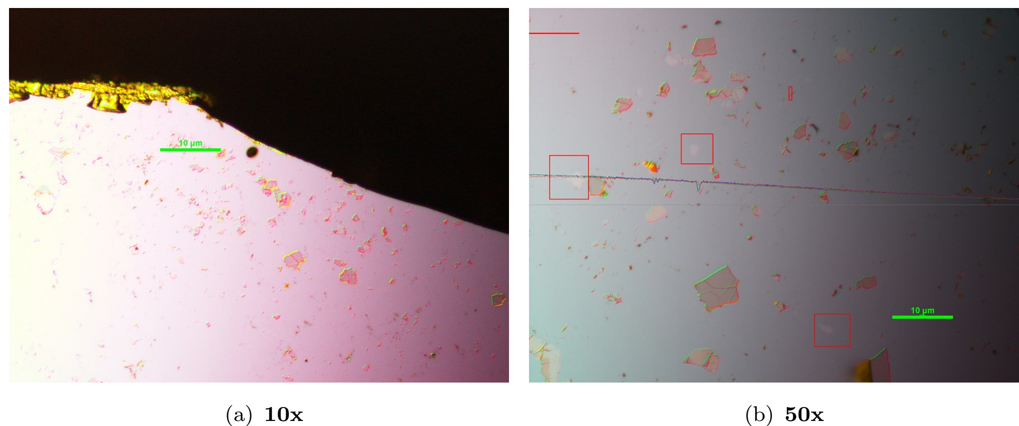

(a) **10x** (b) **50x**

FIGURE 3.3: Optical image of Si wafer after exfoliation of HOPG. Fig(a) shows graphene crystallites are hidden in haystack of thousand of thick flakes. Fig(b) shows two flakes, inside red boxes, with feeble contrast which might be a few-layer graphene.

Characterization of graphene flakes

Morphological characterization using AFM

Figure 3.4 (a, b, c) shows the AFM images of one of the thinnest flake that we could find. The flake has a thickness of 8 nm. Typically, a single layer graphene has a thickness of .35 nm. So this flake consists of around 20 layers of graphene. From visual inspection of the image graphene flake one can clearly see the traces of crumpling and wrinkling of graphene sheets which is inherent to two dimensional materials. In the top right corner of the image, all the graphene layers in flake have folded over leading to doubling of the height in the height profile. Figure 3.4 (c, d, e) shows the zoomed topography of a graphene sheet. Along the line cut

made in Figure 3.4 (d) one can see the atomic steps in stacked layers. The average step size is 0.3 nm which matches with the theoretical value.

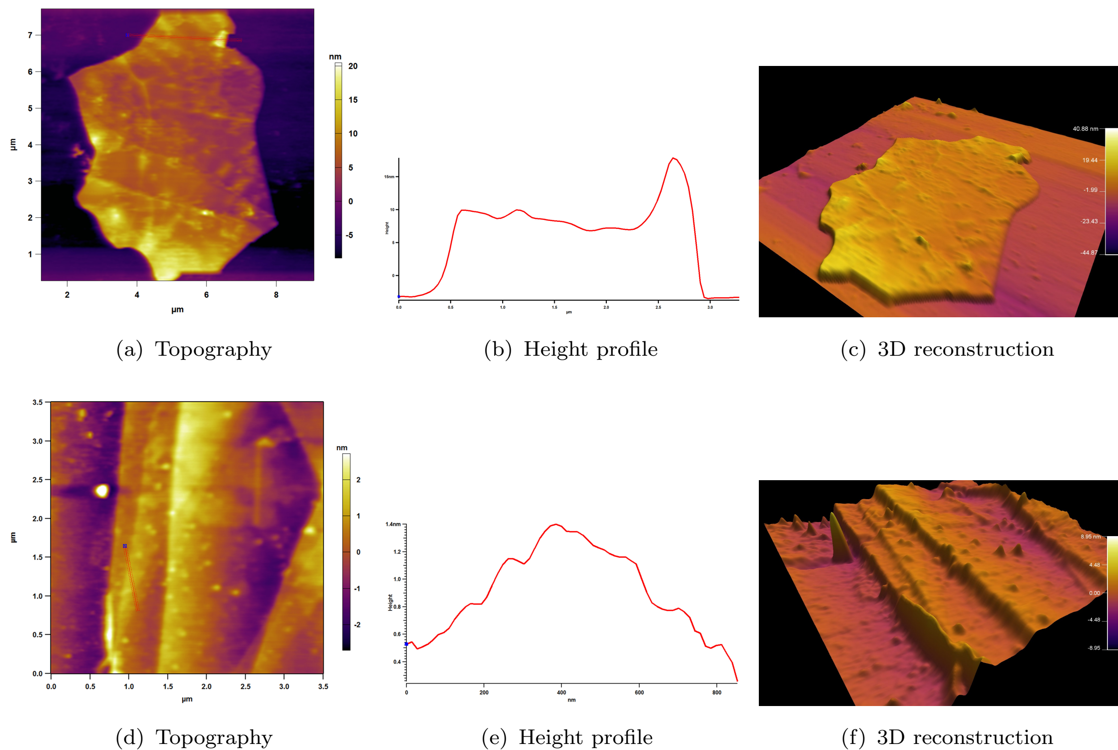

(a) Topography (b) Height profile (c) 3D reconstruction

(d) Topography (e) Height profile (f) 3D reconstruction

FIGURE 3.4: AFM images of multilayered graphene flakes. Fig(a,b,c) show a graphene flake of thickness $8nm$ comprising of about 22 monolayers. Crumpling, wrinkling and folding of graphene is also visible. Fig (d,e,f) show the atomic steps in stacked layers. From Fig(e) atomic step can be measured to be around $0.3nm$.

Raman analysis

Raman spectroscopy is a vibrational technique that is extremely sensitive to geometric structure and bond within molecules. The spectra of graphene or graphite is characterized by two principal bands designated as **G** (*1587 cm-1)* and **2D** (*2710cm-1*) bands[28]. The G band corresponds to the in-plane vibrational mode involving SP_2 hybridised carbon atoms that comprises the graphene sheet. As the number of layers progresses from single layer to multilayer graphene, the intensity of G band increases linearly. The 2D band is the result of two phonon lattice vibration. As the number of layers of graphene increase this band splits into several overlapping bands and broadens. The single layer graphene can be be identified by analysing the ratio of the peak of 2D and G band. For a single layer graphene

this ratio is more than 2. In our case 2D/G ratio was 0.6 which corresponds to multilayer graphene.

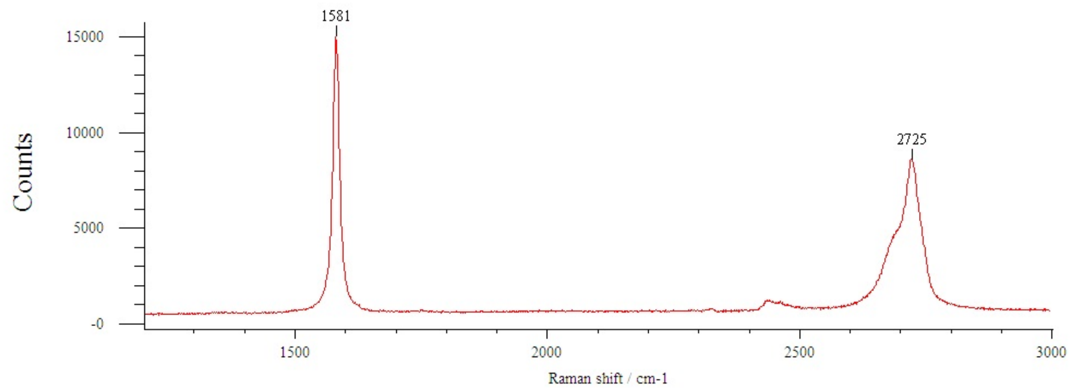

FIGURE 3.5: Raman spectra of a multilayer graphene flake using $512nm$ laser. The I_{2D}/I_G ratio is 0.60 which corresponds to atleast 10 layers.

3.3 Conclusion

We were able to identify graphene flakes up to 20 layers. But unfortunately we could not continue the project as the e-beam lithography required for making electrical contacts to the flake was not available promptly. We look forward to utilize the required facilities and throw some light on the conceived project.

Chapter 4

Artifacts in Atomic Force Microscopy

Scanning probe microscopy like any other microscopies are vulnerable to artifacts and noise which can lead to misrepresentation of the true feature under investigation. In atomic force microscopes, these arifacts have multiple origin including tip, piezo scanners, feedback and electronics. In this chapter I would discuss some of the common artifacts and their possible causes.

4.1 Artifacts due to tip

In AFM, tip senses the surface and generates the topography map which is actually a convolution of tip geometry and the shape of the feature. If the tip is sharper and smaller than the feature to be probed, generated image would be closer to the dimensions of the feature. However if the aspect ratio of the tip is smaller than that of the feature, convolution effect of the tip would be more pronounced. In such a case, for e.g., a feature can appear larger and broader or the depth of a hole would be underestimated. In some cases an image may contain large number of repeating patterns. This particularly happens when the feature on a surface is much smaller than the tip which means that instead of tip scanning feature it is the feature which is scanning the tip. It is common to find triangular structures in the image while scanning nano particles with a silicon tip having triangular cross-section. If the tip is damaged or chipped it can develop multiple heads which can create shadows or ghost images.

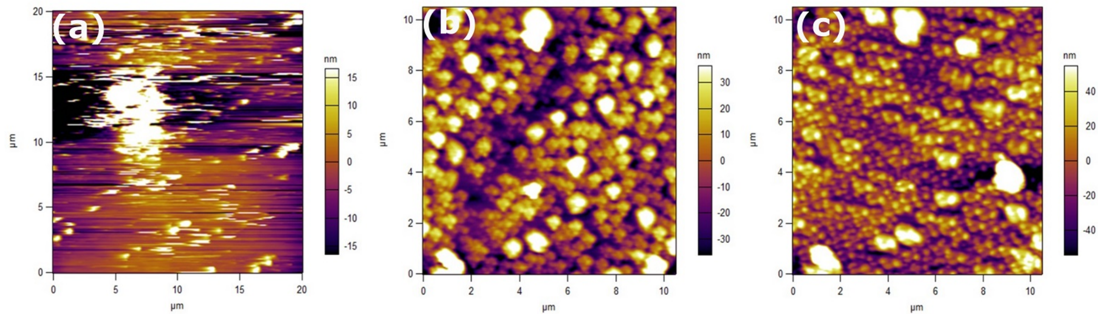

FIGURE 4.1: Artifacts due to tip. (a) Scan lines formation as the tip drags the loosely attached particles along with it. (b) Repeating triangular artifacts due to tip geometry while scanning nanoparticles. (c) Ghost image artifacts due to multiple heads in the damaged tip.

4.2 Artifacts due to piezo scanners

In AFM, piezo-scanners are used to scan sample in X, Y and directions. Piezo-scanners are non linear devices which means they move non-linearly to the applied voltage. Due to this non-linearity while scanning a large area, a large "bow" like background is observed in the AFM image. Further, peizo-scanners are also susceptible to thermal drift which can lead to drift in the scan area. This problem is more prominent while scanning smaller areas.

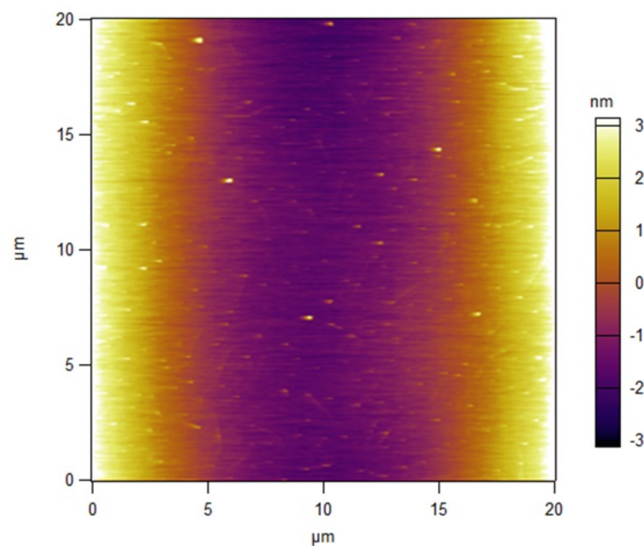

FIGURE 4.2: A bow like background due to non linear behaviour of the piezo

4.3 Artifacts due to electronic noise

Electronic noise show up in the image as high frequency oscillations which look like repeating patterns. This can happen because of several reasons. Firstly, if the sample is not properly grounded and the surface accumulates electrostatic charge it can influence the cantilever deflection. Secondly, if the feedback gain is set too high then it can amplify the ground loop noise and lastly, vibration from floor and acoustics can also influence the measurement. Sometimes, if the surface being scanned is flat then the laser reflected from the cantilever interferes with the part of laser reflected from the surface. This can lead to low frequency undulation in the image.

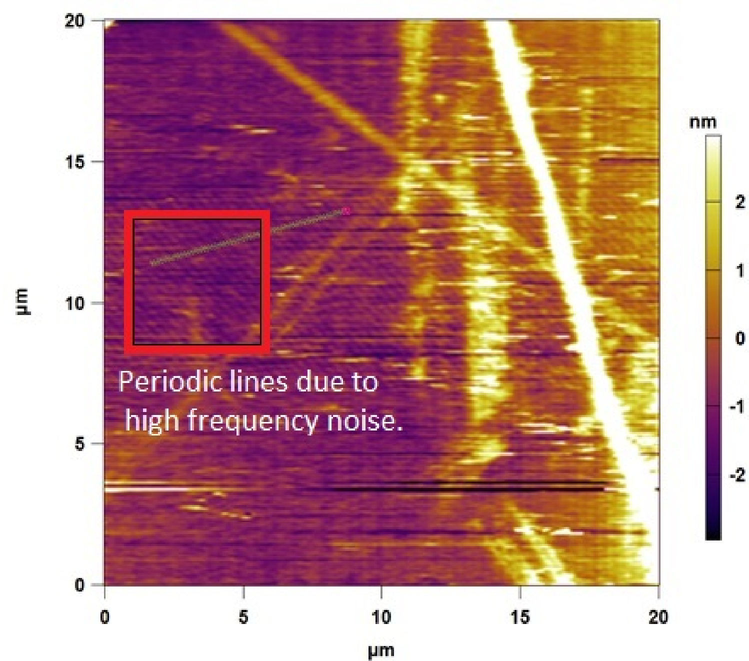

FIGURE 4.3: Electronic noise

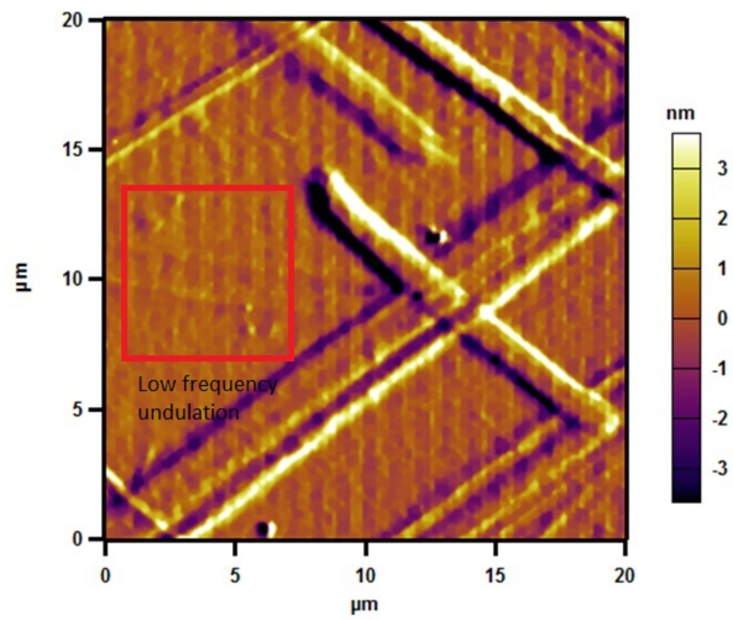

Figure 4.4: Noise due to interference

Chapter 5

Soft Point Contact Device Fabrication

When a current of electrons flows through a macroscopic contact between two metals, it undergoes scattering by not only the local defects in the lattice but also by the elementary excitations like phonons and magnons. This contributes to a measurable voltage drop across the contact which is described by Ohm's law. As the contact size between two conductors decreases, the current-voltage dependence deviates from the ohms law. This is because when the contact size is more than the mean free path of the electron, they routinely undergo scattering, but when it is less than mean free path of the electron, statistical probability of undergoing scattering becomes negligible. In such a scenario, kinetic energy of the electron is a function of the voltage difference across the constriction. This property can be used to extract important spectroscopic information about the energy and momentum of the electron near the fermi energy[19, 29].

The most common method for doing point contact spectroscopy involves pressing a sharp tip into the sample in a controlled manner and then measuring the conductance as a function of voltage across the junction[30]. Here we have used a different technique to make a permanent point contact by device fabrication. This technique involves making a point contact on thin films or bulk material by puncturing a nano-hole in a insulating polymethyl methacrylate (PMMA) layer which is sandwiched between the two samples. Thus two samples comes into electrical contact only through the nano-hole in the intermediate PMMA layer. These devices are simple, versatile and robust as measurements can be performed several

times, and then stored and remeasured. Here we have developed a superconductor (niobium) - metal (gold) soft point contact device (FIGURE 3.1).

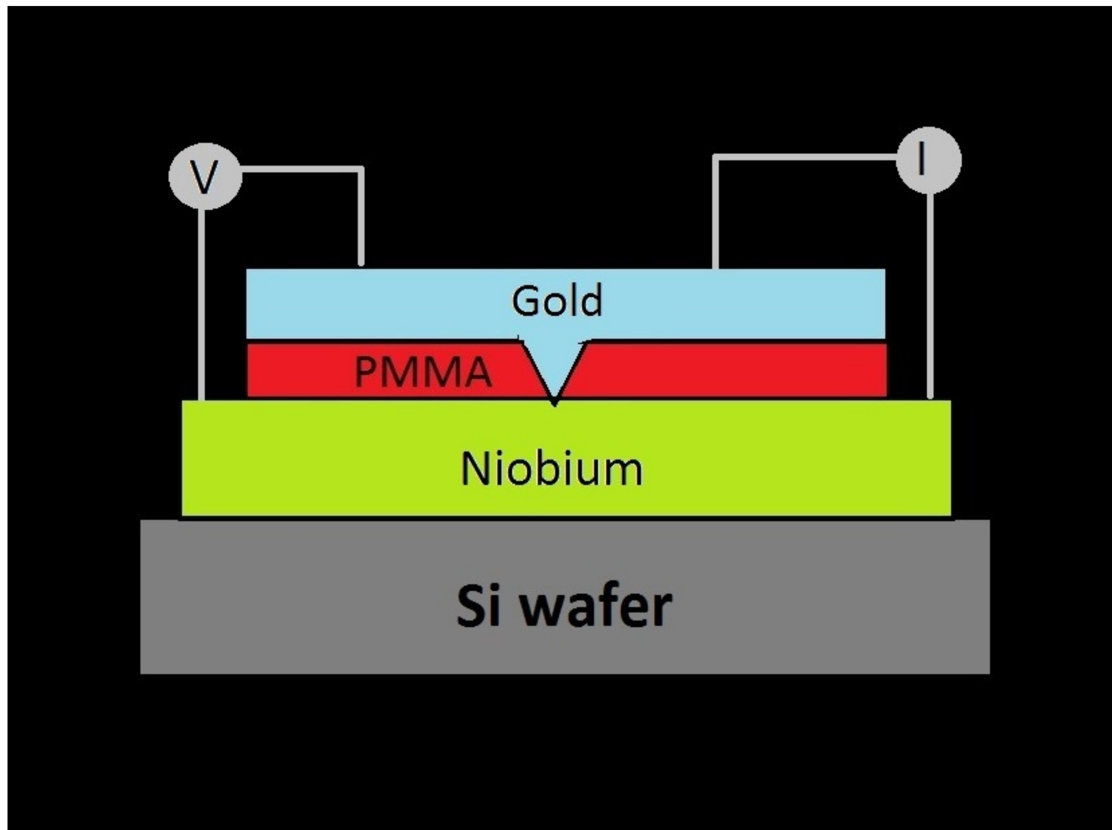

FIGURE 5.1: Schematic of soft point contact device: superconductor (Nb)-metal (Au)

5.1 Method

Synthesis of Niobium thin film

Thin films of niobium (Nb) were prepared on a silicon substrate using DC magnetron sputtering. In this technique, thin films of the desired material is synthesized from its pellet (target) by bombarding it with energetic particles. The cluster of atoms from the target's surface gets ejected due to energy transfer from the bombarded ions. These neutral clusters of atoms travel in a straight line and gets deposited on the surface of a substrate. In order to create energetic ions, a negative potential is applied to the target in high vacuum having continuous metered flow of argon gas in the chamber. The argon atoms get ionised and forms

a gaseous plasma which is trapped by the magnetic field generated from the magnets located behind the target. This ensures that the ions in the plasma hits the target efficiently and eject its atoms. The quality and thickness of the thin film can be tuned by varying the target potential, sputtering time, argon flow rate and substrate temperature.

Before sputtering, it is necessary to clean and anneal the substrate. We sonicated the Si wafer in acetone and isopropyl alcohol for 10 minutes each at 70^0C followed by annealing at 800^0C for 2 hours in vacuum of 10^{-7} mbar. Once the substrate cooled down to ambient temperature, argon was flushed into the chamber and a pressure of 2.1 x 10^{-2} mbar was maintained. Deposition was done for 15 minutes at target potential of 250 V.

PMMA coating

The niobium film was masked from the left and right sides by the kapton tape. This would later be used for making electrical contacts to the film. A layer of PMMA was spin coated on the film at 3000rpm. However, while inspecting the surface with a multimeter, surface was still found to be conducting. To insure that all the surface including microscopic hills in the film are covered with PMMA we spin coated 10 layers on it. After this sample was soft baked at 180 ^{0} C for 1 minute and 45 seconds, so that PMMA layer is rigid enough to maintain the dimensions of any hole indented in it.

Nano hole indentation

To create a hole, a none hole indenter set-up was made (FIGURE 3.2). It has a electrochemically etched sharp tip made from a tungsten wire. This tip is mounted on a peizo scanner which can move along x axis with nano-meter step precession. Sample is placed on fixed vertical stage using silver paint. A bias is applied between the tip and the sample and resistance is measured. Initially, the tip is away from the sample, so resistance is infinite. As the peizo scanner moves the tip towards the sample and finally approaches it, resistance starts to show in the range of several giga-ohms. At this point tip has just came in contact with the insulating PMMA layer. When peizo scanner further pushes the tip into the sample, tip begins to indent the PMMA layer which is marked by corresponding fall in the resistance.

Typically, when the resistance is in the range is 10-50 kω the hole is neither too large nor too small.

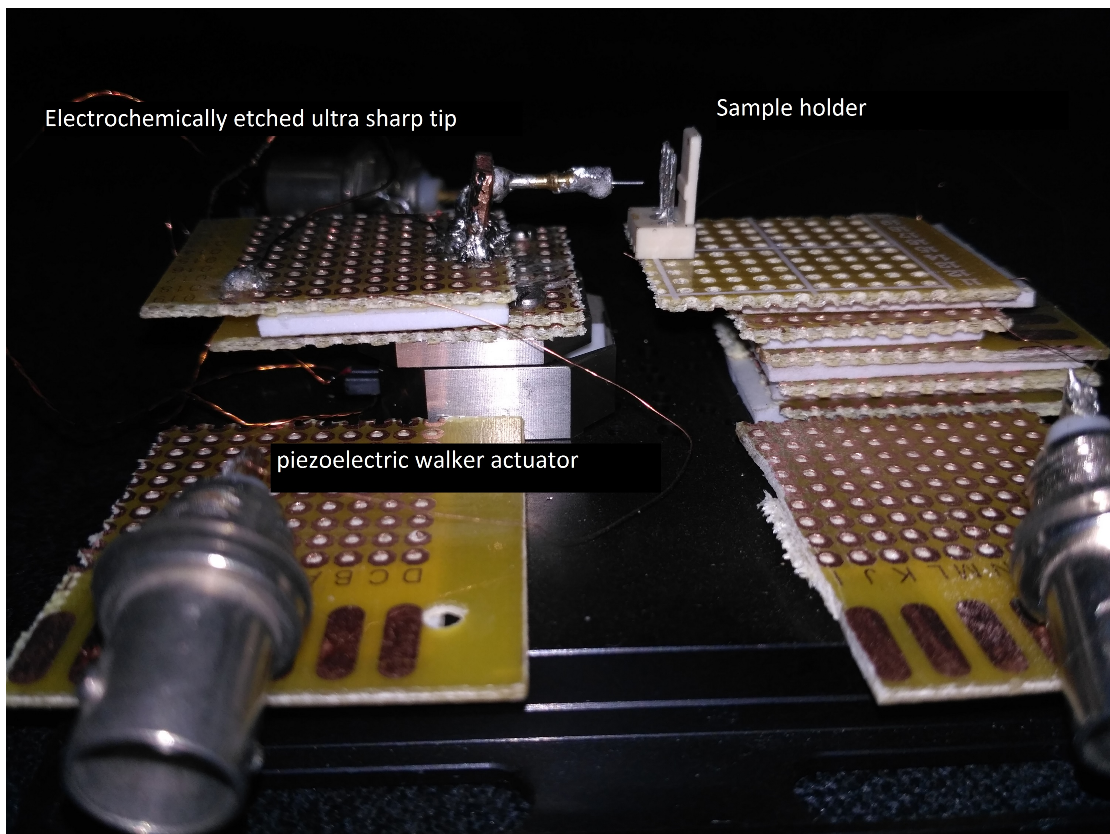

FIGURE 5.2: Nano hole indenter setup.

Gold deposition

Gold is deposited on the indented PMMA coated Nb film using thermal evaporator. In this technique a piece of gold is evaporated in high vacuum condition which condenses on the sample placed near it. This process gives a high quality gold coating.

Electrical contacts

Electrical contacts were made using thin insulating copper wire. Kapton tape, masking the niobium layer, was removed. Wires were scracthed from its ends and then connected to the sample using silver paint. Two connections were made in the top gold layer while other two were made in the masked area.

5.2 Measurements

The measurements were performed in a He-4 cryostat which goes down to 2 K. The DC currentvoltage characteristics at different temperatures were measured by the standard four-probe method. Temperature of the sample was monitored using Lake Shore 350 temperature sensor which was placed just below the device. The voltage was measured using KEITHLEY2000 Multimeter while SRS 830 Lock-in Amplifier was used for implementing AC lock-in modulation technique.

Resistance vs temperature dependence

Resistance vs temperature was measured from 300 K to 2 K. FIGURE 3.3 shows temperature resistance from 2 k to 10 k. Niobium shows a superconducting transition at 6.5 K marked by a sharp fall in resistance to almost zero.

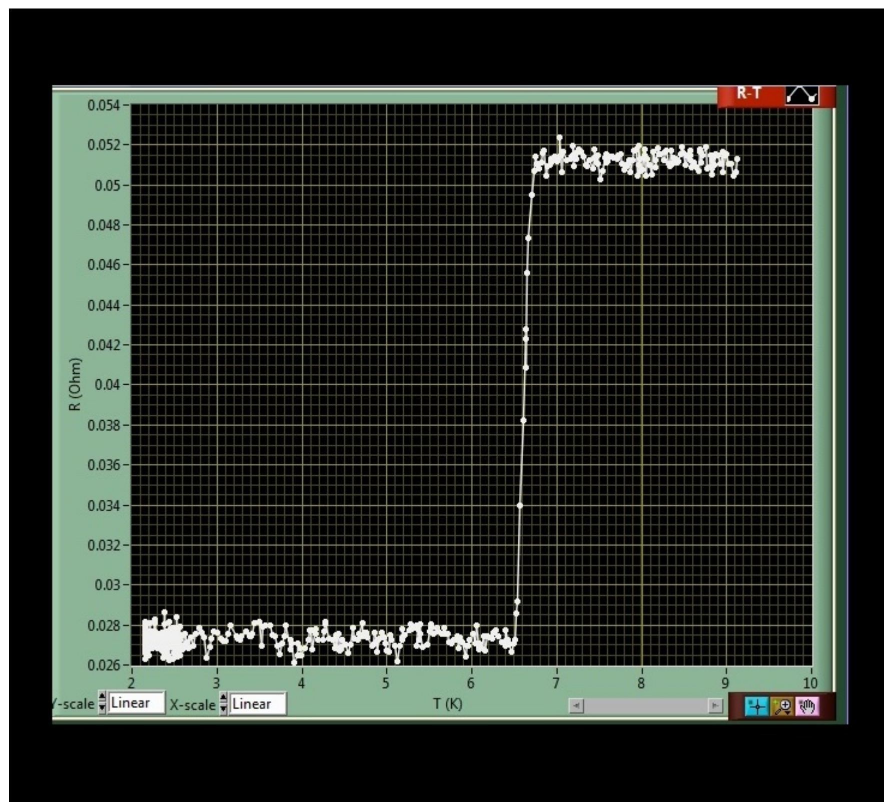

FIGURE 5.3: Resistance vs Temperature dependence. Niobium shows a superconducting transition at 6.5 K

Dependence of differential resistance on temperature

We measured the differential resistance (dV/dI) of the soft point of Nb-Au by a lock-in modulation technique. FIGURE 3.4 shows the measured dV/dI as a function of dc-bias (V) across the Nb-Au junction for a range of temperature from 1.6 K to 7 K in the thermal regime. There are two sharp peaks symmetric about V=0 in the plot corresponding to 1.6 K at $\pm 3.8mV$. These peaks originate when the dc-current flowing through the junction reaches the critical current. For the voltages between $\pm 3.8mV$ there is a dip in the dV/dI due to the transition of Nb to the superconducting state. As the temperature is increased, thermal energy is added to the system. As a consequence superconductivity is broken at a lower value of critical current. This also leads to suppression of sharp transition into metal state as the energy distribution in the particles broadens. Eventually, after a critical temperature dip in the dV/dI vanishes.

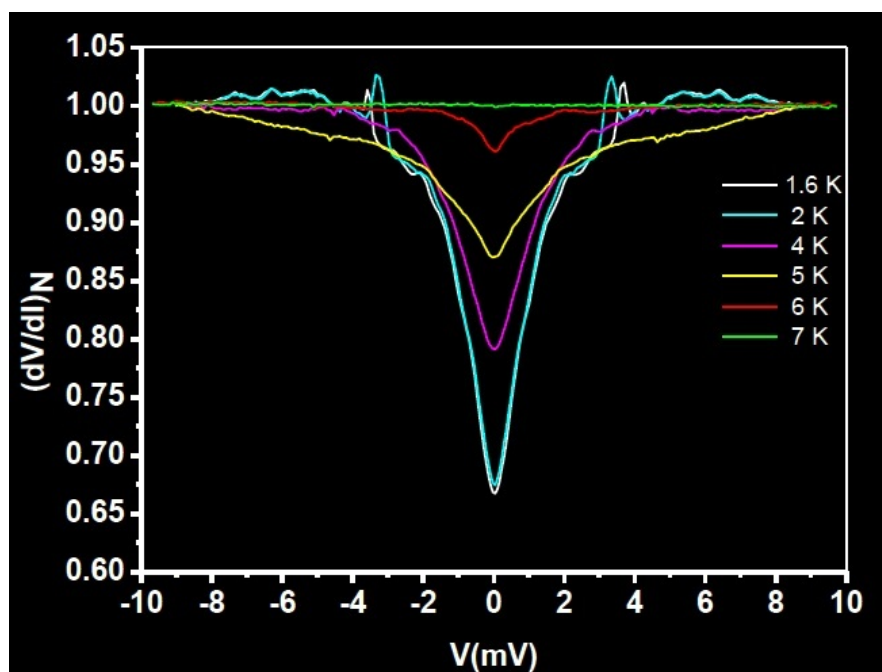

FIGURE 5.4: The temperature dependence of critical current peaks in thermal regime.

Dependence of differential resistance on magnetic field

FIGURE 3.5 shows the evolution of critical current peaks with magnetic field. A magnetic field upto 60 kG was applied using superconducting magnet. The central

dip and critical current in the spectra evolves systematically with magnetic field. We can see in figurexx the superconductivity survives upto H_c= 60 kG.

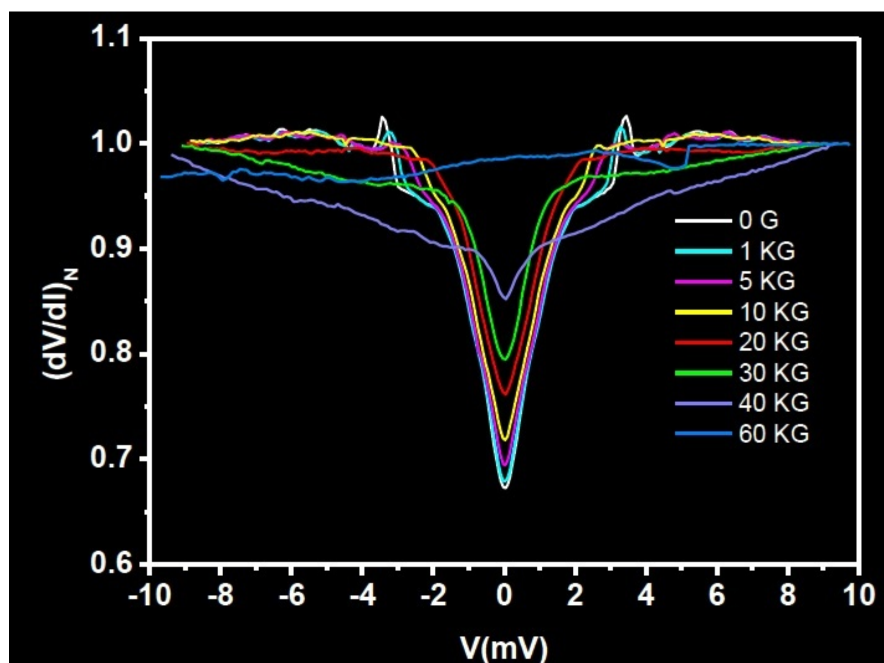

FIGURE 5.5: The magnetic field dependence of the normalised differential resistance (dV/dI)

Chapter 6

Scanning Tunneling Spectroscopy

Scanning tunneling spectroscopy (STS) is a powerful tool to investigate the electronic excitations in real space with atomic precision. The differential conductance (dI/dV) measured by sweeping a dc bias across a tunnelling contact directly probes the local density of states (LDOS) as a function of energy. In the case of superconductors STS can be used to measure the superconducting gap. This is done by fitting the STS data (dI/dV vs V) with the celebrated Dynes formula. In this chapter I would deal with Dynes formula simulation which I have used to fit the spectroscopy data of PdTe2, a conventional superconductor. The code has been developed in Python and can be found in the appendix A .

6.1 Theory

When a positive bias is applied across two electrodes, here to the sample with respect to the tip, separated by a very thin barrier, electrons can quantum mechanically tunnel from occupied state of the tip to the empty state of the sample. Bardeen, Tersoff and Hamann formulated the theory of a current through a tunneling contact where they assumed the tunneling process to be elastic and the net tunneling current can be written as[31, 32]

$$I = I_{t\to s} - I_{s\to t} \tag{6.1}$$

$$= \frac{4\pi e}{\hbar} \int_{-\infty}^{+\infty} |M|^2 N_s(E_s) N_t(E_t) \{ f(E_t,T)[1-f(E_s,T)] - f(E_s,T)[1-f(E_t,T)] dE \} \quad (6.2)$$

where e is the electron charge, M is the tunneling matrix and N_t and N_s are the density of states of the tip and the sample respectively while $f(E,T)$ is the Fermi-dirac distribution[33]:

$$f(E,T) = \frac{1}{(1 + exp(\frac{E}{k_B T})} \quad (6.3)$$

For the bias V, the tip energy can be written as $E_t = E - eV$ and sample energy can be written as E_s=E. Substituting this in the tunneling current:

$$I = \frac{4\pi e}{\hbar} \int_{-\infty}^{+\infty} |M|^2 N_s(E) N_t(E - eV)[f(E,T) - f(E - eV, T)] dE) \quad (6.4)$$

This current is known as the integrated density of states (IDOS). From here one can directly calculate the density of states (DOS) by differentiating the IDOS with respect to V. This gives the differential conductance G(V):

$$G(V) = \frac{dI}{dV} \quad (6.5)$$

When the tunneling junction is between superconductor (sample) and a normal metal (tip), N_t can be treated as a constant function and can be taken out of the integral as metals have a flat density of states in the relevant energy scale where superconducting gap (Δ) is expected. The density of state for a superconductor N_s, as in BCS theory, is given by $N_s(E) = \frac{(E)}{\sqrt{(E)^2 - \Delta^2}}$. However, in practice quasiparticles have a finite life time which causes a broadening of the BCS density of states. Dynes incorporated this effect by introducing a broadening term Γ which takes into account all the nonthermal sources of broadening[34]. Now N_s can written as $N_s(E) = Re(\frac{(E - \iota\Gamma)}{\sqrt{(E - \iota\Gamma)^2 - \Delta^2}})$. The complete dynes formula for the conductance spectra is given by:

$$\frac{d}{dV}(G_N \int_{-\infty}^{+\infty} N_s(E) N_n(E - eV)[f(E) - f(E - eV)] dE) \quad (6.6)$$

Here G_N is the resistance of the tunnel junction for $V \gg \Delta/e$.

6.2 Results

Tunneling spectroscopy (dI/dV vs V) for a superconductor-metal junction has been simulated using Dynes formula. FIGURE 6.1 shows the simulated spectra for a superconducting gap Δ= 320 μ V, broadening Γ = 4 percent of Δ and the temperature T=[0.001K - 5k]. There are two symmetric coherence peaks at $\pm$ 320 muV which evolves with changing the temperature. As the temperature increases, the height of the peaks decrease and finally disappears at 5 K. In the next figure (FIGURE 3.9), I have illustrated the effect of increasing the magnitude of broadening term Γ. As the Γ increases, coherence peaks start to broaden and shrink in height while the superconducting dip smoothens and narrows down.

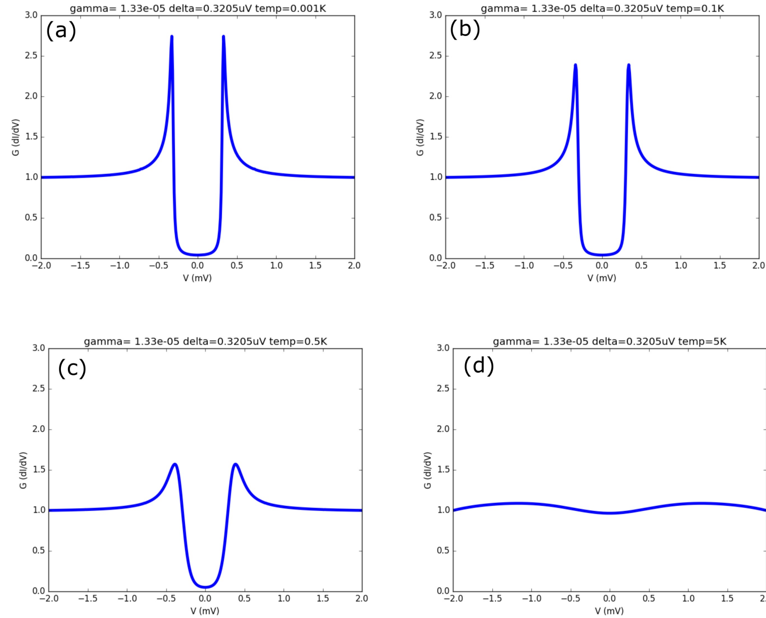

FIGURE 6.1: Evolution of coherence peaks and superconducting dip with increasing temperature

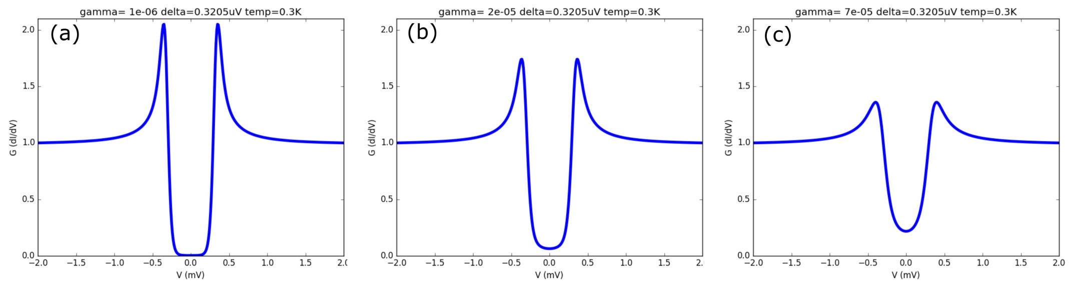

FIGURE 6.2: Evolution of coherence peaks and superconducting dip with Γ

I have also fitted the STS data of $PbTe_2$ with Dynes formula and estimated the Δ. From the fitting we found Δ to be 325 μ eV at 385 mK (FIGURE 6.3).

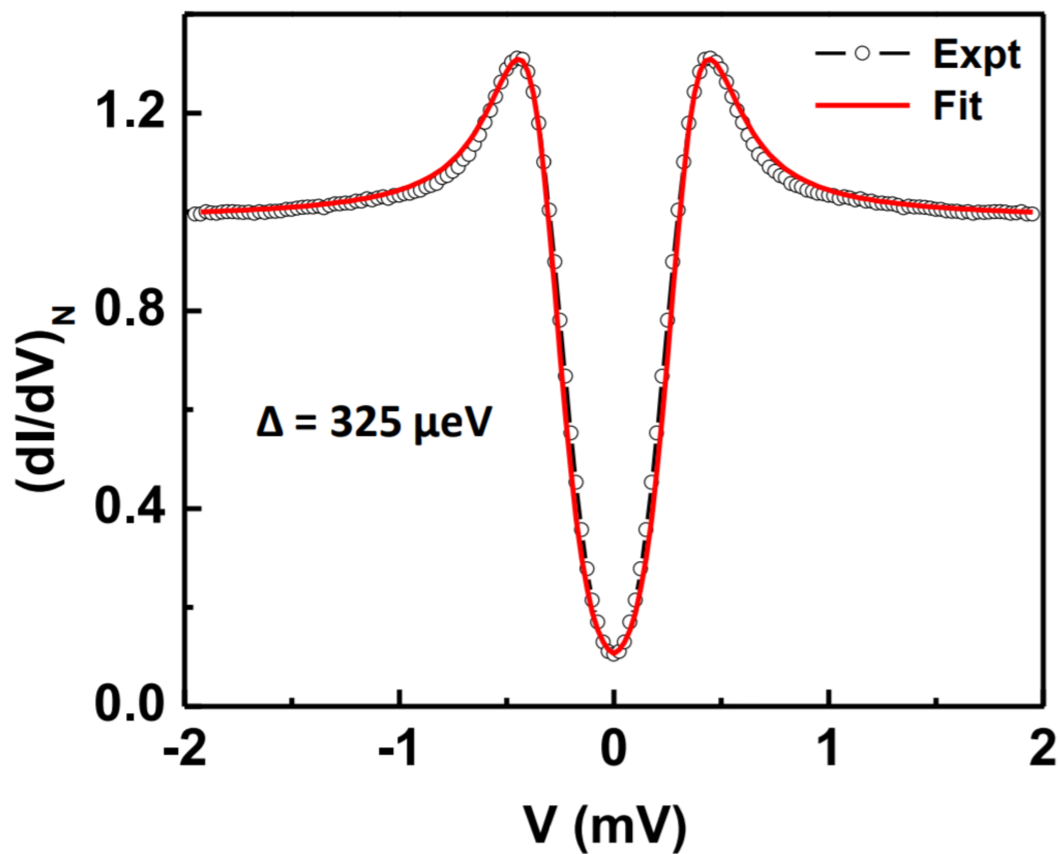

FIGURE 6.3: Experimental STS data of $PbTe_2$ fitted with Dynes equation.

Appendix A

Python code for Dynes fit

```
# -*- coding: utf-8 -*-
"""
Spyder Editor


"""

import numpy as np
import pylab as P
import scipy as S
import scipy.special as SS
import scipy.integrate as SI
import scipy.optimize as SO
import math

from scipy.misc import derivative
import matplotlib.pyplot as plt
import matplotlib

Ef= 0 #fermi energy
k=8.611*10**-5   #bolthzman
 #temperature
e=1

# fit function


def Ns(E,t,d):


    return abs((((np.complex(E,-t)/(np.complex(E,-t)**2-d**2)**.5).real)))

def F(E):
    return 1/(np.exp((E-Ef)/(k*T))+1)

def integrand(E,V,t,d):
   # t,d = args
```

```
    #return Ns(E,t,d)*Ns((E-e*V),t,d)*(F(E)-F(E-e*V))
    return Ns(E-e*V,t,d)*(F(E)-F(E-e*V))


def integration(V,t,d):


    res = S.integrate.quad(integrand,-limit,limit,args=(V,t,d))
    return res[0]

#def vcurve(E, t,d,V):
#     return numpy.vectorize(D(E, t,d,V), excluded=set([1]))

data = np.loadtxt('data.txt')
Vdata= data[:,0]/1000
ydata=data[:,1]
yreverse=ydata[::-1]
temp=(ydata+yreverse)/2
ydata=temp
temp=ydata/10**-4# changing i to g and normalise
ydata=temp/np.amax(temp)
#d=0.000316171435
#t=2.5421*10**-5
d=.000306704374293
t=2.153039725*10**-5
T=0.8
limit=0.1
num=33
basename='dec 7 data'
def grad(Vdata,t,d):


    integrated=np.zeros(len(Vdata))
    i=0;

    for V in Vdata:
        integrated[i]=integration(V,t,d)/1000000

        i+=1
    grad=np.gradient(integrated,Vdata[1]-Vdata[0])
    temp=np.amax(abs(grad))
    return abs(grad/temp)
    #return integrated


if(1==2):
    plt.figure(1)
    plt.plot(Vdata,ydata,'ro')
        #plt.plot(Vdata,(grad(Vdata,t,d)),linewidth=4.0)
    plt.plot(Vdata,(grad(Vdata,t,d)),linewidth=4.0)
    plt.ylabel('G ')
    plt.xlabel('V (eV)')
    plt.title("gamma= "+str(t)+' delta='+str(d)+' limits=+-'+str(limit) +'temp='+str(T))
```

```
    plt.savefig(basename+str(num))
##


if(2==4):
    plt.figure(1)
    plt.plot(Vdata,ydata,'ro')
    for i in range(1,5):
        plt.plot(Vdata,(grad(Vdata,t+i*.05*t,d)),linewidth=.2)  #ten percent more
        plt.plot(Vdata,(grad(Vdata,t-i*.05*t,d)),linewidth=.2)  #ten percent less
        plt.plot(Vdata,(grad(Vdata,t,d+i*.05*d)),linewidth=.2)  #ten percent more
        plt.plot(Vdata,(grad(Vdata,t,(d-i*.05*d))),linewidth=.2)  #ten percent less
        plt.plot(Vdata,(grad(Vdata,t,d)),linewidth=1)
    plt.ylabel('G ')
    plt.xlabel('V (eV)')
    plt.title("gamma= "+str(t)+' delta='+str(d)+' limits=+-'+str(limit))
    plt.savefig(basename+str(num))
##


if(1==1):
        p,q=S.optimize.curve_fit(grad,Vdata,ydata,p0=(t,d),maxfev=10000000)
        fitp=grad(Vdata,p[0],p[1])

        plt.figure(1)
        plt.plot(Vdata,ydata,'ro')
        plt.plot(Vdata,fitp,linewidth=4.0)
        plt.ylabel('G ')
        plt.xlabel('V (eV)')
        plt.title("gamma= "+str(p[0])+' delta='+str(p[1])+'T='+str(T) +' limits=+-'+str(limit))
        plt.savefig(basename+str(num))
```

Bibliography

[1] Scanning probe microscopy. *Center for probing the nanoscale.*

[2] SRINIVASA M. SALAPAKA and MURTI V. SALAPAKA. Scanning probe microscopy. *IEEE CONTROL SYSTEMS MAGAZINE.*

[3] Joachin Loos. The art of spm: Scanning probe microscopy in materials science.

[4] Mfp-3d spm user guide. user guide 1.

[5] H.K. Wickramasinghe Y. Martin, C.C. Williams. *J. Appl. Phys. 61, 4723.*

[6] True non-contact mode. *Nanotechnology Solutions Partner.*

[7] K. Kjoller V.B. Elings Q. Zhong, D. Innis. *Surf. Sci. Lett. 290, L688.*

[8] Yogesh Singh and P. Gegenwart. *Phys. Rev. B* ***82**, 064412*, 2010.

[9] A. N. Kolmogorov T. Lancaster I. I. Mazin S. J. Blundell P. G. Radaelli Yogesh Singh P. Gegenwart K. R. Choi S. W. Cheong P. J. Baker C. Stock S. K. Choi, R. Coldea and J. Taylor. *Phys. Rev. Lett.* ***108**, 127204*, 2012.

[10] Huibo Cao Bryan C. Chakoumakos Jaime A. Fernandez-Baca Radu Custelcean T. F. Qi O. B. Korneta Feng Ye, Songxue Chi and G. Cao. *Phys. Rev. B* ***85**, 180403(R)*, 2012.

[11] G. Jackeli and G. Khaliullin. *Phys. Rev. Lett.* ***102**, 017205*, 2009.

[12] G. Jackeli J. Chaloupka and G. Khaliullin. *Phys. Rev. Lett.* ***105**, 027204*, 2010.

[13] A. Vishwanath X. Wan, A. M. Turner and S. Y. Savrasov. *Phys. Rev. B* ***83**, 205101(R)*, 2011.

[14] Y.-B. Kim W. Witczak-Krempa, C. Gang and Annu. L. Balents. *Rev. Condens. Matter Phys.* ***5**, 57*, 2014.

[15] D. A. Pesin and L. Balents. *Nat. Phys.* ***6**, 376*, 2010.

[16] X. Liu et al. *Phys. Rev. B* ***83**, 220403(R)*, 2011.

[17] J. Reuther-T. Berlijn R. Thomale W. Ku-S. Trebst Yogesh Singh, S. Manni and P. Gegenwart. *Phys. Rev. Lett.* ***108**, 127203*, 2012.

[18] R. Thomale J. Reuther and S. Trebst. *Phys. Rev. B* ***84**, 100406(R)*, 2011.

[19] Yu. G. Naidyuk and I.K. Yanson. Point-contact spectroscopy. *Springer*, 2003.

[20] M. Daghofer Jeroen van den Brink Y. Singh P. Gegenwart S. Winter, A. A Tsirlin and R. Valent. *J. Phys.: Cond. Matter* ***29** 493002*, 2017.

[21] Y. Yu and S. Qin. *e-print arXiv:1202.1610.*

[22] Ann. A. Kitaev. *Phys. (N.Y.)* ***321**, 2*, 2006.

[23] A. Vishwanath I. Kimchi. *ArXiv:13033290*, 2013.

[24] J. Kunes? Xiao-Liang Qi Shou-Cheng Zhang A. Shitade, H. Katsura and N. Nagaosa. *Phys. Rev. Lett.* ***102**, 256403*, 2009.

[25] Moyuru Kurita Ryotaro Arita Youhei Yamaji, Yusuke Nomura and Masatoshi Imada. *Phys. Rev. Lett.* ***113**, 107201*, 2014.

[26] G.M.Fox R.J.Cava J.W.Krizan, J.H.Roudebush. *Materials Research Bulletin* ***52**, 162*, 2014.

[27] P. R. Wallace. The band theory of graphite. 1947.

[28] Mark Wall. The raman spectroscopy of graphene.

[29] P. Wyder A.M. Duif, A.G.M Jansen. Introduction to superconductivity. *J. Phys. Condens. Matter 1, 3157-3189*, 1989.

[30] Lucas et al Janson. Undergraduate experiment in superconductor pointcontact spectroscopy with a nb/au junction. *American Journal of Physics 80.2, p. 133.*

[31] J. Bardeen. Tunneling from a many-particle point of view. *Phys. Rev. Lett., 6 (57)*, 1961.

[32] J. Terso and DR. Hamann. Theory and application for the scanning tunneling microscope. *Physical review letters, 50(25):1998(2001)*, 1983.

[33] M. Tinkham. Introduction to superconductivity. *McGraw-Hill, New York*, 1996.

[34] V. Narayanamurti R.C. Dynes and J. Pm Garno. Direct measurement of quasiparticle-lifetime broadening in a strong-coupled superconductor. *Physical Review Letters, 41(21):1509(1512)*, 1978.